Space Science Reviews (2025) 221:56
https://doi.org/10.1007/s11214-025-01181-7

Constraining the Mass and Energy of Enceladus' Dissipation Systems

Carly J.A. Howett[1] · **Georgina M. Miles**[2] · **Lynnae C. Quick**[3]

Received: 9 October 2023 / Accepted: 7 June 2025

Abstract

NASA's Cassini mission revealed endogenic activity at the south pole of Saturn's moon Enceladus. The activity is concentrated along four fractures in Enceladus' ice shell, which are much warmer than their surroundings and the source of Enceladus' plumes. This work provides a review of the current state of knowledge of the energy and mass lost by Enceladus through this activity. Specifically, we discuss the composition of the plumes, along with their spatial and temporal variation. The mass flux loss predicted for the three plume constituents (gas, dust and charged particles) is reviewed and a total mass flux of ejected material that subsequently escapes Enceladus is estimated to be 2.1×10^{11} kg over a Saturn year. Given that Enceladus' ocean is predicted to be 10^{19} kg this loss is sustainable in the very long term ($\sim$1.5 billion Earth years). However, unless a resupply mechanism (such as serpentinization) exists molecular hydrogen is expected to be depleted within $\sim$1 million Earth years. The difficulty in determining Enceladus' current heat flow is outlined, along with the advantages and disadvantages of the various techniques used to derive it. We find a robust lower limit for Enceladus' exogenic production is 7.3 GW. Tidal heating models show endogenic emission of this level is sustainable, and Enceladus may have long-term near-surface heating (a result supported by studies of Enceladus' geology). Finally, we offer suggestions for future observations, instrumentation, and missions. Enceladus remains a high-priority target for NASA, and as such it is highly likely that we will return to study this enigmatic world. Hopefully these missions will answer some of the questions that remain.

Keywords Satellites · Surface · Plume · Tides

1 Introduction

Along with Europa and Triton, Enceladus belongs to a small family of cryovolcanically active moons in our solar system (Fagents et al. 2022). The activity occurs inside Enceladus' South Polar Terrain (SPT) along four fractures, or sulci, commonly known as Tiger Stripes

---

✉ C.J.A. Howett
carly.howett@physics.ox.ac.uk

[1] Atmospheric, Oceanic and Planetary Physics, University of Oxford, Oxford, UK

[2] Southwest Research Institute, Boulder, CO, USA

[3] NASA Goddard Space Flight Center, Greenbelt, MD, USA

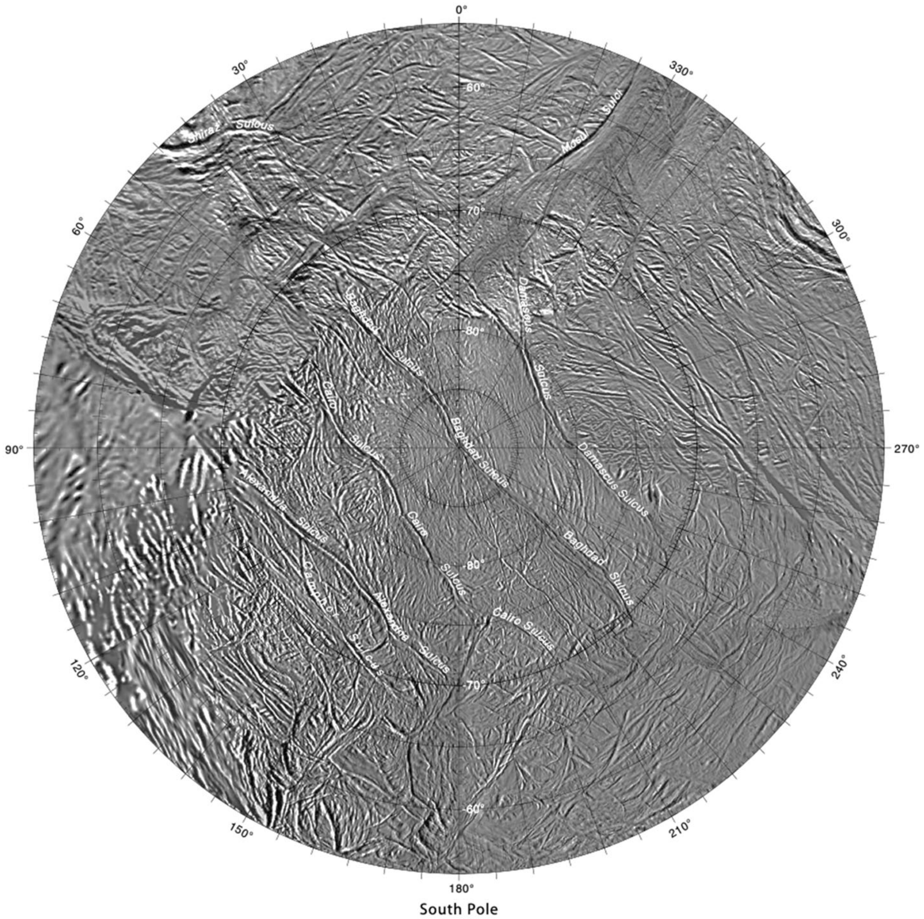

Fig. 1 Enceladus' South Pole, with the major sulci nomenclature included. Image from (USGS 2015)

(Fig. 1). The fractures are named after cities or countries referred to in The Arabian Nights, and the four largest fractures are Damascus, Baghdad, Cairo, and Alexandria Sulcus (see Fig. 1 for locations). These fractures are approximately 130 km long, with a central trough 2 km wide and 0.5 km deep. They are the source of both the plumes (Fig. 2) (Helfenstein and Porco 2015; Porco et al. 2014, 2006a; Spitale et al. 2015; Spitale and Porco 2007) and Enceladus' thermal emission (Fig. 3) (Spencer et al. 2006).

Enceladus' south polar plumes represent the only manifestation of its cryovolcanic activity. This contrasts with Europa and Triton, that display a variety of flow-like features and landforms that are indicative of effusive eruptions (Croft et al. 1995; Fagents 2003; Kattenhorn and Prockter 2014; Lesage et al. 2021; Miyamoto et al. 2005; Prockter et al. 2017; Quick et al. 2022, 2017). Triton's surface is also littered with features that may have been emplaced because of explosive cryovolcanism, including pitted cones, and ring and pit paterae and their deposits (Croft et al. 1995; Helfenstein et al. 1992).

Enceladus' plumes were seen to be continuously active throughout the Cassini mission (e.g., Ingersoll et al. 2020), and are expected to be at least decadal-long, starting well before Cassini's arrival (Jurac and Richardson 2001). By contrast Europa's putative plumes appear

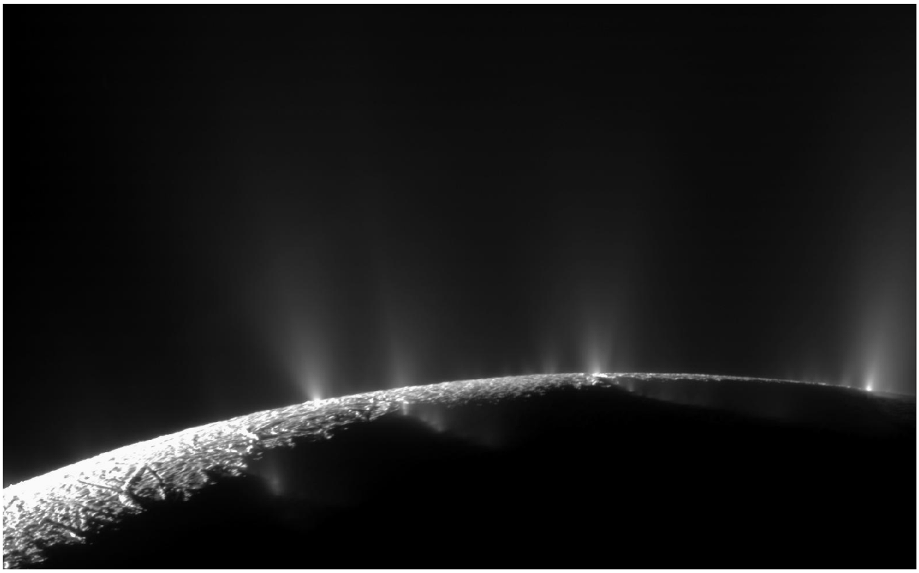

Fig. 2 A mosaic of two Cassini ISS NAC images taken of Enceladus' plumes on 21st November 2009. Image credit: NASA PIA11688

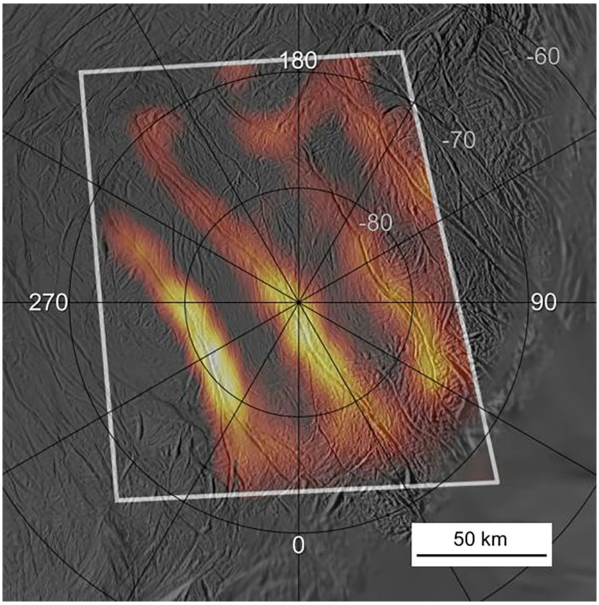

Fig. 3 Heat flow across Enceladus' South Polar Terrain. The warmest temperatures (bright yellow) are at ∼180 K, and the background (uncolored inside the white box) is at ∼72 K. Image credit: NASA PIA10361

to be someone elusive. While ground- and space-based telescopic observations have provided evidence for Europa's plumes, they may be sporadic with large, 200 km tall, plumes being infrequent outliers (Paganini et al. 2019; Rhoden et al. 2015; Roth et al. 2014a,b; Sparks et al. 2017, 2016). This is consistent with modeling (Fagents 2000; Quick et al. 2013) and past searches for plumes in the Galileo dataset (Phillips et al. 2000) which sug-

Table 1 A comparison of properties for Mars', Triton's, and Enceladus' plumes. Table adapted from Table 1 of Hansen et al. (2021) using values from Hansen et al. (2021) and references therein

	Mars	Triton	Enceladus
Erupting Volatile	CO_2	N_2 or H_2O	H_2O
Surface Gravity (m/s^2)	3.72	0.779	0.113
Plume Height (km)	0.08	8	1500
Plume Height Normalized to Triton Gravity (km)	2	8	60
Source Vent Diameter (m)	< 1	< 3000	~ 9
Exit Velocity (m/s)	20-300	20-40	450
Vapor Mass Flux	150 g/s	up to 400 kg/s	200 kg/s
Particle Mass Flux	30-150 g/s	< 10 kg/s	~ 50 kg/s
Eruption Temperature (K)	140	38-42	76-170
Eruption Duration	< 2 hours	1-3 years	continuous

gest that plume activity on Europa may be small-scale and transient in nature. We note that the community remains divided on whether Europa does indeed have plumes, and recent JWST observations found no evidence for strong active plumes (Villaneuva et al. 2023) at the time of their study. However, for the purposes of this review we assume Europa's plumes exist and use their constraints to better contextualize those of Enceladus.

Triton's plumes are quite different to both those on Europa and Enceladus. The activity was discovered in images of Triton returned by Voyager 2, and shown to be four N_2-rich plumes located between 50°S and 57°S. These plumes reached heights of up to 8 km above the surface (Soderblom et al. 1990). The initially favored eruption hypothesis for Triton's plumes was that they were solar driven (Kirk et al. 1995), similar to seasonal jets on Mars (Thomas et al. 2011). However, the discovery and characterization of Enceladus' plumes has led to a reevaluation of plausible hypotheses for eruptive venting on Triton (Hansen and Kirk 2015). Indeed, Hansen et al. (2021) note that the mass flux of Triton's plumes is more akin to the plumes at Enceladus than to the Martian jets (Table 1). In addition, new analyses by Hofgartner et al. (2022) suggest that neither the locations of the plumes, or of their fan-like deposits, strongly support the solar-driven model. While Kirk et al. (1995) invoked a cryovolcanic model for the formation of Triton's plumes, a separate endogenic eruption model was also proposed, in which the base of a polar cap composed of N_2 ice is melted by internal heat, and plumes form when the melt is exposed to the surface (Brown and Kirk 1994).

Venting on Enceladus, Europa, and Triton may be driven, at least partially, by tides and tidal stresses (e.g., Nimmo et al. 2014; Nimmo and Spencer 2015; Rhoden et al. 2015). Enceladus' plumes appear brightest at apoapsis— a time during its orbit when extensional tidal stresses are the greatest, allowing the fractures to open (Hedman et al. 2009; Hurford et al. 2007). Similarly, cryovolcanic activity may occur on Europa during times in its orbit when extensional stresses facilitate the opening of fractures and the exposure of subsurface water (Fagents et al. 2022). Internal energy from obliquity tides could drive cryovolcanism on Triton (Nimmo and Spencer 2015). Nevertheless, ocean-derived materials that participate in cryovolcanic eruptions on Europa and Triton may experience a more complex path to the surface compared to cryovolcanic materials on Enceladus. Owing to its small size, low surface gravity and thin south polar ice shell, ocean-based fluids erupt directly through south polar fissures (Čadek et al. 2016; Manga and Wang 2007; Nakajima and Ingersoll 2016; Postberg et al. 2011). Indeed, the presence of molecular hydrogen, salts and SiO_2 in

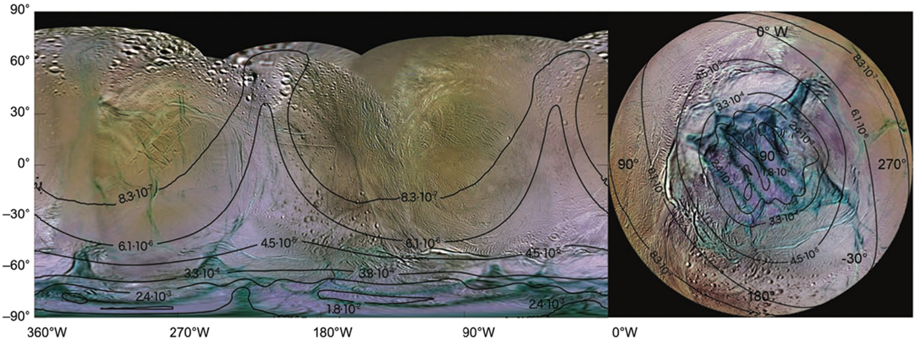

Fig. 4 Color map of Enceladus using ISS GRN/UV3, IR3/GRN and IR3/UV3 for RGB color (Schenk et al. 2011). Overlaid are the plume fallout predictions from Southworth et al. (2019). Image credit: Postberg et al. (2018)

Enceladus' plumes indicate that plume material emanates from an internal ocean that is in direct contact with a rocky mantle (Hsu et al. 2015; Postberg et al. 2011). Conversely, owing to their larger masses, thicker ice shells and higher surface gravities, cryovolcanic materials on Europa and Triton are likely to be sourced from discrete liquid reservoirs or melt lenses within their icy shells (Fagents 2003; Hofgartner et al. 2022; Schmidt et al. 2011).

Models of the predicted distribution of Enceladus plume deposits (Kempf et al. 2010; Southworth et al. 2019) have a strong spatial correlation with Enceladus' surface color change (Schenk et al. 2011) and changes in the water ice distribution (Postberg et al. 2018; Scipioni et al. 2017). From these works it is believed that the plume material that doesn't escape Enceladus' gravity falls back on its surface in two "wedge" shapes centered approximately along 45°W and 225°W (Fig. 4). Recent work has revealed no large-scale surface changes due to the emplacement of plume fall-out on Europa (Schenk 2020), modeling has shown that deposits emplaced by putative large Europan plumes may be difficult to identify (Quick and Hedman 2020). However, one exception may be the low-albedo deposits along ridges and other lineated features on Europa, which may have been emplaced during episodes of explosive cryovolcanism (Fagents 2000). On Triton, surface alteration by plume fallout is easy to spot, with over 120 fan-shaped dark deposits associated with plume activity being seen against the surrounding brighter surface. So many deposits suggest that plume activity could be a common occurrence on Neptune's largest moon (Hansen et al. 1990; Kirk et al. 1995).

Regardless of where their cryovolcanic materials originate, the mass- and energy-loss created by plumes have shaped these worlds. In the case of Enceladus the plume material has covered not only its surface, but sustains the E-ring, and coats and brightens the surface of its neighboring satellites (Verbiscer et al. 2007). The rest of this article delves into both the mass and energy loss Enceladus experiences from its activity. There is a particular emphasis on constraining the magnitude of these losses, their implications for Enceladus' interior, and the insights they offer for models of geological and internal processes on the icy moons.

While the energy loss in the SPT associated with the plumes and cryovolcanic activity via latent heat is significant, by far the principal mechanism of heat loss from the energy created by tidal heating is conduction of heat from the ocean through the ice shell. At a significantly lower intensity, summed over the surface of Enceladus it is estimated to be 5-8 times the energy associated with the plumes (Hemingway and Mittal 2019; Čadek et al. 2016; Spencer et al. 2018). At present we can only predict this heat loss using models of ice shell thickness (from gravity, topographic and libration data) and assumptions about the structure and properties of the ice shell to conduct heat. The longevity of Enceladus' ocean is currently unknown but will be governed by the balance of heat generated within and heat lost via global conduction and the more acute cryovolcanic activity in the SPT.

2 Observations of Enceladus' Mass Flux

2.1 Introduction

The predominant mass flux loss mechanism on Enceladus is the ejection of plume material that erupts from fissures in the South Polar Terrain (SPT). The discovery of Enceladus' plumes was arguably one of the most groundbreaking moments of the Cassini mission, and constraining the plumes' properties quickly became one of the mission's highest priorities. This is because it is hypothesized that the plume composition can shed light on the composition of and conditions of Enceladus' potentially life-supporting sub-surface ocean. The plume ejection has two parts: diffusive emission from along the fractures, sometimes referred to as curtains (Spitale et al. 2015), and from the collimated emission from the $\sim$100 discrete jets (Porco et al. 2014). We use the term plume to describe both these parts.

Enceladus' plume is comprised of three components: solid (dust) particles, gas, and ions. While water is the major constituent of each of these components their individual composition and size varies. Variation is also seen both spatially and temporally. Solid particles are the heaviest components, and as such are most difficult to accelerate to speeds above Enceladus' escape velocity with only 5-10% (by mass) escaping (Postberg et al. 2018). Most of the particles fall back down to coat Enceladus' surface in clearly distinguishable patterns (Fig. 4). However, the lighter neutral gas and charged particles are ejected at such high velocities that they almost all entirely escape Enceladus (Hansen et al. 2008). The escaping particles go on to populate the E-ring (Ingersoll and Ewald 2011; Kempf et al. 2010, 2008; Porco et al. 2006a) and the charged particles are rapidly coupled into Saturn's magnetosphere. So, plume material is found not just in the plume, but also in the E-ring and on Enceladus' surface.

2.2 Instruments Able to Measure Mass Flux and Composition

Cassini was well equipped to study Enceladus' activity with both in situ and remote sensing instrumentation. Both instrumentation types were used to determine the composition of the plume's vapor, solid and charged particles. In this section we briefly describe the instrumentation that was used to make these detections, along with their advantages and limitations.

2.2.1 Solid Particles (CDA/CAPS/VIMS)

The Cosmic Dust Analyzer (CDA) (Srama et al. 2004), Cassini Plasma Spectrometer (CAPS) (Young et al. 2004), the Visible and Infrared Mapping Spectrometer (VIMS) (Brown et al. 2004) and the Imaging Science Subsystem (ISS) (Porco et al. 2006b) all constrained the composition of the plume's solid particles. CDA and CAPS are in situ instruments, while VIMS and ISS remotely sensed the plumes, measuring their composition along its line of sight.

CDA is an impact ionization detector that works by ionizing dust and ice grains that impact its detector's metal target plate at high speed (>1 km/s). A time-of-flight mass spectrometer (TOF-MS) then produces a mass spectrum of the cations present. The mass resolution ($^m/_{\Delta m}$) varies from ∼10 at 1 u (where u is the unified atomic mass unit) to ∼50 at 200 u (Postberg et al. 2006). CDA recorded a few hundred spectra of Enceladus' plume, and many thousands of Saturn's E-ring (Postberg et al. 2018).

CAPS had three sensors: Electron Spectrometer (ELS), Ion Mass Spectrometer (IMS), and the Ion Beam Spectrometer (IBS) (Young et al. 2004). ELS and IMS were primary used to observe the charged nanograins in Enceladus' plume. ELS is a hemispherical top-hat electrostatic analyzer, which was employed during the Enceladus plume flybys was used to detect the direction and energy per charge of negatively charged nanograins. ELS could detect grains with a mass to charge ratio (m/q) of $10^3 - 10^4$ u/q, which made it sensitive to grains sizes between the small neutral gas grains and charged particles, and the larger (>0.4 μm diameter) macroscopic solid ice particles. Postberg et al. (2018) provides full operational details for ELS in the plume. CAPS' IMS provided electrostatic E/q analysis of positive ions between 1 and 34,700 eV/e and included a time-of-flight system for composition (m/q) analysis.

VIMS had both visible (VIS) and infrared (IR) channel which provided sensitivity over its 0.25 to 5.1 μm spectral range, with an effective field of view (iFOV) of 0.5 by 0.5 mrad. The two channels were illuminated via independent telescopes, that were typically operated in conjunction with one another to provide a single spectral cube. As Enceladus' plume is strongly forward scattering, with a low optical depth, it was challenging for VIMS to remotely observe. However, VIMS was able to constrain the plume characteristics by using occultation measurements.

ISS was Cassini's imaging device, made of two framing cameras: a narrow (NAC) and wide (WAC) angle cameras with FOVs of 0.35° and 3.5° across respectively. In both cameras the light was detected by a 1024 by 1024 Charge-Couple Device (CCD). The NAC had a pixel scale of 6 μrad/pixel, while the WAC's was ∼60 μrad/pixel. Filter wheels allowed the camera to span from 200 to 1100 nm.

2.2.2 Gas Phase (UVIS/INMS)

The Ultraviolet Imaging Spectrograph (UVIS) (Esposito et al. 2004) was composed of an Extreme UltraViolet (EUV) and Far Ultraviolet (FUV) spectrograph, a High-Speed Photometer (HSP) and a Hydrogen Deuterium Absorption Cell (HDAC). EUV and FUV covered 563 to 1182 Å and 1115 to 1912 Å respectively. UVIS is a remote sensing instrument, that detected neutral gases in the plume by looking for absorption features in stellar and solar occultations in order to provide the composition integrated through the line of sight between UVIS and the star.

The Ion and Neutral Mass Spectrometer (INMS) (Waite et al. 2004) was a dual-ion source quadrupole mass spectrometer. It covered a mass-to-charge range of 0.5 to 8.5 and 11.5 to 99.5 u. It could operate in a closed- and open-ionization configuration, meaning both inert and reactive species and ions could be detected.

2.2.3 Charged Particles (CAPS and MIMI)

As described above, CAPS used ELS and IMS to measure the negatively and positively charged particles in the plume respectively. The Magnetospheric Imaging Instrument (MIMI) (Krimigis et al. 2004) had three sensors: Low-Energy Magnetospheric Measurement System (LEMMS), Charge-Energy Mass Spectrometer (CHEMS) and Ion and Neutral

Camera (INCA). LEMMS measured the velocity, direction and number of electrons, ions and protons that struck its detector. CHEMS measured both the charge and composition of particles that struck its detector, and INCA was able to image high velocity atoms.

2.3 The Composition and Variability of Enceladus' Plume

2.3.1 Solid Particles

As already mentioned, most of the plume particles fall back onto Enceladus' surface (Postberg et al. 2018), but 5-10% are able to escape Enceladus and sustain the E-ring (Ingersoll and Ewald 2011; Postberg et al. 2018). So, this means that the plume's solid particle composition can be either directly measured or inferred from E-ring studies.

Solid particles have been detected by CDA, CAPS and VIMS, in both the plume and the E-Ring.

However, since the E-ring is much larger than the plumes the in-situ instruments had more opportunity to sample it than the plumes. Most of the compositional information on plume/E-ring ice grains comes from CDA (Postberg et al. 2018), which showed the grains can be broadly separated into three types:

- Type 1 particles ($\sim$65% of E-ring particles) are almost pure water ice, with very low concentrations of alkali salts (Na/H_2O ratio of 10^{-7}) (Postberg et al. 2009).
- Type 2 particles ($\sim$25% of E-ring particles) are larger than Type 1 but roughly the same composition with some additional organic species (which manifest as 27 u to 31 u and/or 39 u to 45 u species) (Postberg et al. 2008). The ratio of organics to non-organics, and the concentration of silicate and salt varies between the particles.
- Type 3 particles ($\sim$10% of E-ring particles) are also much larger than Type 1 particles but are compositionally very different to the other types having a pronounced sodium signature (Na/$H_2O > 10^{-3}$).

VIMS provided additional insight into the structure of the water of Enceladus' plume, showing that the water ice emerging from Cairo, Baghdad and Damascus was all crystalline (Dhingra et al. 2017). This implies that the water plume particles were formed at temperatures > 130 K.

The concentration of these particles within the plume varies on short (diurnal/orbital), medium (monthly) and long (yearly) timescales. Since Enceladus is tidally locked to Saturn it takes the same time to orbit Saturn as it does to rotate (i.e., a day is the same length of time as its orbit). So, the terms orbital and diurnal can be used interchangeably. However, short-term variation in plume concentration varies as a function of its position (Hedman et al. 2013; Ingersoll et al. 2020; Ingersoll and Ewald 2017; Nimmo et al. 2014) (and not time of day) so we default to using the term orbital.

Hedman et al. (2013) used VIMS data to study changes in Enceladus' plume over its orbit. A position in an orbit is defined by mean anomaly (MA), which is the time from pericenter (when Enceladus is closest to Saturn) multiplied by 360° and divided by the orbit period. So pericenter is at 0° and apocenter (when Enceladus' is furthest from Saturn) has a mean anomaly of 180°. Hedman et al. (2013) also showed that the horizontal integrated plume brightness is three times greater at apocenter than pericenter, and that the orbital position appears to affect particle velocity (with lowest velocities at apocenter) but not the particle size distribution.

These initial findings were confirmed using ISS observations, which found the plume's peak brightness to occur at apoapse, notably with a scale height that didn't vary with orbital

Fig. 5 Slab density verses mean anomaly (orbital position) on Enceladus. From Ingersoll et al. (2020)

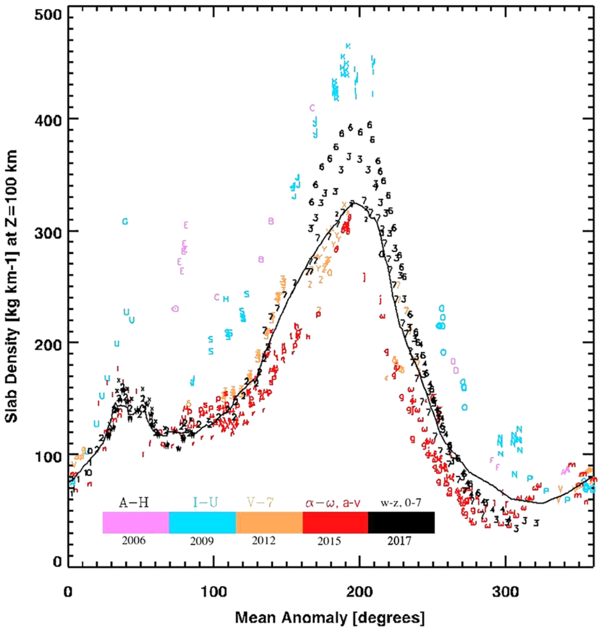

position or plume brightness (Nimmo et al. 2014). This implies that (in contrast to Hedman et al. 2013) the particle velocities are constant. These results supported the theory that tidal stresses control Enceladus' plume emission (Nimmo et al. 2014). Further modelling showed that the location of Enceladus' jets, the location of warm surface regions and diurnally varying tidal stresses is coincident, and they could be sufficient to open Enceladus' fractures all the way from the surface to the sub-surface ocean (Porco et al. 2014).

A follow up ISS study observed a four-fold increase in plume brightness at apocenter than pericenter (Ingersoll and Ewald 2017). This was followed by the most comprehensive study of ISS images to date (Ingersoll et al. 2020), which analyzed 2415 ISS observations to find that the plumes change in brightness with orbital position is indeed very complex:

- The large maximum occurs slightly after apocenter (the maximum is at MA∼200°)
- There is a secondary maximum in the plume brightness, made up of two peaks with an MA of 25° and 60°.

This same study also found evidence of the plumes changing on monthly timescales. ISS observations of jets taken at the same mean anomaly were used to track their output and showed about half of the ten jets observed had changed over the course of a month (Ingersoll et al. 2020). Some of the jets turned on, while others disappear. Porco et al. (2014) also showed jet activity varied with time, but couldn't correlate the observed activity an individual jet to Enceladus' stress field. Instead, they suggest individual geysers turn off when they become clogged with ice from condensed vapor.

Between 2007 and 2017 there was a factor of two decrease in the plume brightness (Fig. 5) (Ingersoll et al. 2020; Ingersoll and Ewald 2017). This long-term brightness change is best fitted by a pair of sinusoids with a period of ∼4 years and ∼11 years (Porco et al. 2018), which agrees with the known tides on Enceladus from its resonance with Dione. Ingersoll et al. (2020) see evidence for variation in the launch velocity of plume particles, from their stable 2009-2015 value to an elevated one in 2017. This means their results are consistent with Hedman et al. (2013) but not with Nimmo et al. (2014).

While the total brightness of the plumes varies temporally, the composition of the plumes varies spatially. Generally, Type 3 grains are more concentrated close to the surface while Type 1 particles were less so, and Type 2 show a more complex variation pattern (Postberg et al. 2011). One explanation is that the ejection speeds of the smaller Type 1 grains are faster than the larger Type 3 ones (Postberg et al. 2011), perhaps due to a radius-dependent frictional force in the vent (Schmidt et al. 2008). Thus, the larger Type 3 particles are less able to escape Enceladus' gravity than the smaller Type 1 particles and are more highly concentrated close to the surface (Hedman et al. 2009; Kempf et al. 2008). This could also explain why Type 1 particles are more dominant in the E-ring (Khawaja et al. 2017), because they are more able to escape.

Type 2 particles appear to vary with the ground-track of the observations, being most pronounced over Damascus Sulcus (Postberg et al. 2011). Combined UVIS and VIMS analysis showed the dust/gas mass ratio above Baghdad and Damascus Sulci is about an order of magnitude higher than that of Alexandria and Cairo Sulci (Hedman et al. 2018). Surfaces around Damascus are known to have strong organic-ice features (Brown et al. 2006). Thus, these results support Damascus having a strong dust signal that is notably rich in organics.

2.3.2 Vapor

During Cassini's mission UVIS and INMS made numerous observations of Enceladus' plume vapor. Early observations established the gas was predominately water (Hansen et al. 2006; Waite et al. 2006) with a column density of $1.5\text{x}10^{16}$ H_2O molecules cm^{-2} over an altitude of 7 to 30 km (Hansen et al. 2006). INMS initially constrained the remainder of the gas plume to be ~3% CO_2, 4% unknown species with mass 28 u (CO, N_2 and C_2H_4 being some of the candidates), <0.5% NH_3, and trace amounts of acetylene and propane (Waite et al. 2006).

Analysis of UVIS data was able to provide some insight onto possible mass 28 u species. The data provided an upper limit of CO (<0.9%), N_2 (0.5%) and found evidence of C_2H_4 but couldn't define a mixing ratio (Hansen et al. 2006, 2017). However, later observations made by INMS in their open-source mode gave no detection at 28 u. In open source mode the particles are ionized without interaction with the instrument's walls, which leads to less fractionation of heavier particles. So perhaps the source of 28 u is actually a fragmentation product (e.g., CO or C_2H4) of a heavier organic molecules, rather than a specific 28 u mass one. This open-source data also enabled the mixing ratio of H_2 to be determined (0.4 to 1.4%) (Waite et al. 2017).

During the Cassini mission INMS refined the process of taking their data, finding a sweet spot between the fast speeds required for high signal-to-noise and the effect those high speeds had on producing fragmented species from high-speed wall impacts. Three encounters (E14, E17 and E18) in 2011 and 2012 particularly benefited from this work. They were taken at the sweet spot, with a relative speed of ~7.5 km/s (Postberg et al. 2018) and an altitude of 75 to 100 km above the fractures. Figure 6 shows the plume gas composition derived from data taken during the three flybys. The results are strongly consistent with one another, providing a confident determination of the gas species. The final volume mixing ratios are: H_2O (96-99%), CO_2 (0.3-0.8%), CH_4 (0.1-0.3%), NH_3 (0.4-1.3%) and H_2 (0.4-1.4%) (Waite et al. 2017). Compositional variations in the gas plume were observed, but are not currently linked to individual sources (Magee and Waite 2020, 2017; Waite et al. 2017)

The plume gas mass flux appears to not change notably with time. Analysis of five occultation observations made by UVIS showed the bulk water vapor coming from Enceladus

Fig. 6 Mass spectrum from INMS taken during E14 (light grey), E17 (black) and E18 (medium grey). From Postberg et al. (2018)

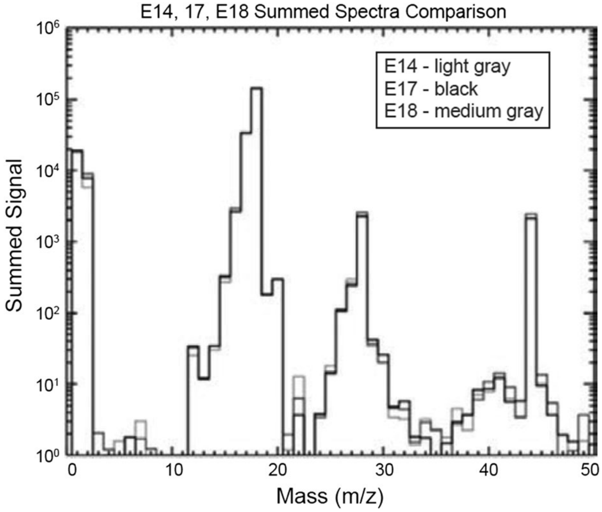

Fig. 7 The mass-dependent behavior of high-velocity molecules emitted by Enceladus' jets. It is assumed that all molecules are emitted at the same supersonic velocities. The figure shows that for species in thermal equilibrium the amount of spreading depends on their mass. From Perry et al. (2015)

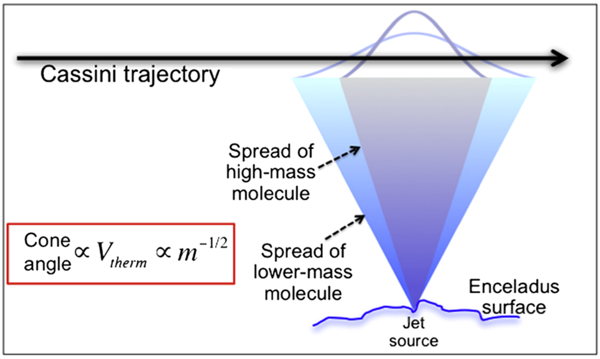

was approximately constant with a surface density varying between 0.9×10^{16} cm^{-2} and 1.5×10^{16} H_2O molecules cm^{-2} (i.e. ±15%) and did not display correlation with orbital position (Hansen et al. 2017). However, interestingly the mass flux from individual gas jets was shown to significantly vary (Hansen et al. 2017; Teolis et al. 2017).

Spatial variations of the concentration of neutral gas within the plume are substantial. The gas is emitted from jets at supersonic velocities and at slower speeds from the diffuse emission (Hansen et al. 2008; Teolis et al. 2017). The fast-moving gas molecules leaving a jet will spread as a function of their molecular mass with low-mass molecules spreading more than high-mass ones (assuming they have the same eruption velocity and are in thermal equilibrium) (Fig. 7). Analysis of INMS data showed that this results in a spatial variation in the plume's composition (Perry et al. 2015), with heavy species (e.g., CO_2) spreading less than lighter ones (e.g., H_2 and H_2O) (Yeoh et al. 2015). INMS typically sampled the plume at altitudes between 50 and 100 km altitude. Through these encounters the spreading angle was shown to vary from 10° to 45°, depending on the temperature, velocity and mass (Hurley et al. 2015; Perry et al. 2015).

2.3.3 Charged Particles

The charged particles can be split into three types: charged nanograins, positive ions, and negative ions. The positive and negative ions are largely formed within the plume by charge exchange (Cravens et al. 2011). These charged particles, once formed, are eventually lost to Saturn's magnetosphere, becoming part of the ambient plasma torus (Johnson et al. 2006; Tokar et al. 2006). Therefore, their ability to inform on Enceladus' surface and sub-surface is limited.

The charged nanograins were observed by CAPS in Enceladus' plume (Jones et al. 2009). These grains are larger than the neutrals and other charged species, but smaller than the solid ice grains. They are indirectly assumed to be icy (Coates et al. 2010a,b; Hansen et al. 2011, 2008; Postberg et al. 2011; Waite et al. 2017), and carry both positive and negative charges (Jones et al. 2009) caused by electron impact in the plume itself (Hill et al. 2012).

RPWS and CAPS ELS both saw an increase in plasma density close to Enceladus (Coates et al. 2013; Morooka et al. 2011). The plume's positive ions were studied by CAPS IMS and found to be primarily composed of water group ions (O^+, OH^+, H_2O^+ and H_3O^+) (Young et al. 2005). H_3O^+ is formed via charge exchange, when magnetospheric ions interact with plume H_2O to form H_2O^+ and H_3O^+ (Cravens et al. 2011). Negative water ions (OH^-, O^-, H^-) are also observed in the plume

(Coates et al. 2010a). They are expected to have been formed inside the plume itself by dissociative electron attachment and have a short lifetime.

2.4 What Is the Total Mass Loss of the Plume?

There are multiple lines of evidence to support the hypothesis that plumes are a long-lived phenomenon. For example, they were active during every encounter Cassini had with Enceladus' SPT (2005-2017). Their material supports the E-ring, and without it then it is expected that the current E-ring would disperse in decades (Jurac and Richardson 2001). Finally, surface heating and cratering records (see Spencer et al. 2006) point to activity lasting much longer than ∼1000s of years. Depending on the plume flux such activity could result in significant mass loss. Since the vapor, solid and ions are detected separately so are their mass loss rates, and in this section we explore the mass flux of these different plume particles separately.

UVIS data initially constrained the H_2O vapor from eruptions to be occurring at a rate of 150 to 350 kg/s (Hansen et al. 2006). Subsequent occultations supported these results, finding rates between 170 and 250 kg/s (Hansen et al. 2017, 2011). These initial estimates assumed ice temperatures which gave the gas a thermal velocity much higher than Enceladus' escape velocity (240 m/s), implying all the vapor escapes Enceladus. So, these rates imply that over each Saturn year (29.4 Earth years) Enceladus is losing $1.4 \times 10^{11} - 3.2 \times 10^{11}$ kg of H_2O through the gas plumes alone.

There is large uncertainty in the flux of solid particles emitted from Enceladus, with estimates varying from 3 to 65 kg/s (Dong et al. 2015; Ingersoll and Ewald 2011; Kempf et al. 2018, 2010; Schmidt et al. 2008). Assuming a conservative 20 kg/s (Kempf et al. 2018) this means 1.9×10^{10} kg of solid material is ejected from Enceladus' over the course of a Saturn year (6.3×10^8 kg over an Earth year). If 10% escapes Enceladus (Postberg et al. 2018) then the particle mass loss from Enceladus is 1.9×10^9 kg per Saturn year (6.3×10^7 kg over an Earth year). This is a sizeable amount but notably lower than the vapor loss.

Charged particles are expected to form in the plume by charge exchange, and it is difficult to determine their specific contribution to the total mass loss. Despite this some estimates do

Table 2 Summary of the mass flux estimates for the total vapor, solid and charge particles in Enceladus' plume in the literature (unless otherwise indicated)

Plume type	Mass flux (kg/s)	Reference
Vapor		
	150 - 350	(Hansen et al. 2006)
	100	(Schmidt et al. 2008)
	200	(Hansen et al. 2011)
	180 - 250	(Hansen et al. 2017)
H_2 Only	0.02 – 0.01	(Waite et al. 2017)
Solid		
	0.04	(Porco et al. 2006a)
	0.2	(Spahn et al. 2006)
	5	(Schmidt et al. 2008)
	50	(Ingersoll and Ewald 2011)
	20	(Postberg et al. 2018)
Charged Particles		
Nanograins	15-65	(Dong et al. 2015)
Negative and Positive Charged Particles	5.6	(Hill et al. 2012; Kempf et al. 2018)
Total Plasma	100	(Tokar et al. 2006)

exist. For nanograins the mass loss is expected to be between 15 kg/s and 65 kg/s (Dong et al. 2015; Kempf et al. 2018). The loss of positive and negative ions is expected to be lower, at 5.6 kg/s (Hill et al. 2012; Kempf et al. 2018). These charged particles are expected to escape Enceladus along field lines bent by Saturn's electromagnetic field (Dong et al. 2015; Hill et al. 2012). Assuming a conservative estimate of 15 kg/s for nanograins and 5.6 kg/s for the ions then Enceladus loses 1.9×10^{10} kg of charged particle material over the course of a Saturn year (6.5×10^{8} kg over an Earth year).

The mass loss estimates described in this section are summarized in Table 2, showing that by far the largest mass loss is from the vapor. If mass fluxes of 200 kg/s are assumed for the vapor (Hansen et al. 2011), 20 kg/s for the solid particles (Kempf et al. 2018), 15 kg/s for the nanograins (Dong et al. 2015), and 5.6 kg/s for the charged ions (Postberg et al. 2018) then the total mass ejected is 241 kg/s, or $\sim 2.2 \times 10^{11}$ kg over a Saturn year (7.6×10^{9} kg per Earth year). If everything escapes Enceladus, except for 90% of the solid particles, then the total mass lost is 223 kg/s, or $\sim 2.1 \times 10^{11}$ kg per Saturn year (7.0×10^{9} kg per Earth year). If Enceladus' ocean is $\sim 10^{19}$ kg (Glein and Shock 2010) such loss rates are sustainable for ~fifty million Saturn-years (~1.5 billion Earth years).

Another constraint on the longevity of Enceladus' activity comes from the loss of molecular hydrogen (H_2), which has been estimated to be between 1×10^{9} to 5×10^{9} mol per year, equivalent to 0.02 to 0.1 kg/s, or 2.0×10^{6} to 1.0×10^{7} kg/year (Waite et al. 2017). Models indicate that the H_2 concentration in the ocean sourced plume will be between 10^{-7} to 10^{-4} mols $(\mathrm{kg}\ H_2O)^{-1}$ (Postberg et al. 2011, 2009). So, an ocean of $\sim 10^{19}$ kg (Glein and Shock 2010) will not be an adequate reservoir of molecular hydrogen in less than one million Earth years (Waite et al. 2017), unless a resupply mechanism exists (such as serpentinization).

2.5 What Does the Mass Loss Tell Us About Enceladus' Interior?

The salt in the Type 3 particles and the minor component of plume gases (CO_2, NH_3, CH_4, H_2, heavy hydrocarbons and silica) provide constraints on Enceladus' ocean composition and dynamics. The leading explanation for this composition is that their source is a liquid water ocean in direct contact with a porous core (Hsu et al. 2015; McKinnon 2015; Postberg et al. 2009). This is consistent with the presence of the minor species, which require hydrothermal cycling between the interior and ocean/ice (see summary chapters by Glein et al. 2018 and Postberg et al. 2018 to explain their presence).

The question then becomes how do these particles form? One option is that they are formed by bubbles bursting at the ocean surface (from evaporation or upwelling of gasses). The spray that results can then be transported upwards by the vapor into space (Postberg et al. 2009). If this hypothesis is correct then the Type 3 grains are direct samples of the subsurface ocean, providing a direct constraint of the composition and salinity of Enceladus' ocean (0.5%) (Postberg et al. 2018).

Conversely the small Type 1 grains, which are almost pure water-ice, are likely to be sublimated ice or evaporated ocean water. The particle's trace sodium levels support the latter explanation, but it could be a mixture of them both (Postberg et al. 2009). This initial vapor then condenses into solid ice grains, a process that requires the vapor to pass through regions of local supersaturation. Such supersaturation conditions could be met by the fractures narrowing into small passageways. This process results in smaller ice grains than the freezing of ocean spray (which can then be accelerated to higher speeds by the escaping gas than their larger counterparts) and can explain the compositional differences between the Type 1 and Type 3 grain sizes.

Enceladus' surface tidal stresses can be constrained by the observed orbital variability of Enceladus' plumes. When the fractures are under compression they will be pressed together (or perhaps even shut), which is likely to reduce the material able to escape. The reverse is true in tension (fractures are pulled apart probably making it easier for material to escape). Current models of Enceladus' surface tension (e.g., Hurford et al. 2007 and Nimmo et al. 2007) show that fissures are expected to be under tension at apocenter and compressed at pericenter, which is in keeping with the brightest plumes being seen at apocenter (Hedman et al. 2013; Nimmo et al. 2014). Berne et al. (2024) showed strike-slip motion on Enceladus could explain the double peak observed in diurnal variations of jet activity, and also matches the tiger stripe's observed heat signature.

The $\sim$monthly variation in jet activity can constrain the fracture size and ice deposition rates. If some of the plume's particles freeze onto the fracture walls as it ascends through the fractures this would both seal up the fracture, and release latent heat. Models of this process, that are able to explain the surface temperature observed, suggest that a crack 5 to 7.5 cm wide could seal in a few months (Nakajima and Ingersoll 2016).

2.6 What Constraints Does This Mass Loss Have on Models?

The observed variation in plume particle output on a variety of timescales indicates the venting process is a complex one. We know very little of the ocean-to-surface plumbing system, which could be anything between distributed porous flow through the ice to direct channels. However, any such model would have to explain the observed temporal variations. The orbital variability alone provides a large source of questions, such as how do wider fractures lead to more plume particles travelling at lower velocities, but with the same size distribution as those emitted by narrower fractures? Why does the particle density change over Enceladus' orbit, while the bulk gas density is (by comparison) constant? Why is the velocity a minimum when the flux is a maximum? How is the secondary peak in particle emission formed, is it due to emission from cross-cutting fractures as suggested by Ingersoll et al. (2020), or something else? Do cracks eventually get sealed by the freezing out of plume particles on the fracture walls? Do they ever reopen? Or more fundamentally, how do they start? Any proposed solution to these questions must also be able to explain longer term plume activity and variability. For example, it is important to determine whether Dione's induced 4- and 11-year tides are really able to cause the trends in plume variation observed. They also must address the long-lived nature of the activity, as all evidence points towards the plume activity being a long-term phenomenon.

The composition of the plumes sets some interesting constraint for interior ocean models. The sodium and potassium salts in the plume (Postberg et al. 2011, 2009) provides a strong constraint on how the salt-carrying plume particles are formed. For example, models that predict vapor is from the sublimation of ice have difficulty explaining their presence, since the ice is expected to be almost pure water-ice, salt free (e.g., Cooper et al. 2009; Kieffer et al. 2006; Loeffler and Baragiola 2009; Nimmo et al. 2007). Instead, the salts are better explained by liquid water models, which allow a subsurface ocean to be in direct contact with a rocky core. The water dissolved salts from the rocks, and eventually go onto be frozen at the surface into droplets that retain their salt content (Postberg et al. 2011). The timescale for this process is not well understood. Hsu et al. (2015) inferred it would take particles several months to transport through Enceladus' ocean. While Ames et al. (2025) use ocean models to show a stratified ocean cannot be made from seafloor to ice shell at Enceladus' polar regions, and thus any hydrothermal products will take upwards of 100s of years to reach the plume (unless the ice shell is not in quasi-equilibrium)

SiO_2 particles will grow to sizes larger than those observed over thousands of years (Spencer et al. 2018). So, the nano-sized silica particles point to a process that is ongoing, rather than one that's completed by reaching the maximum size of particles. If these models of silica growth are right then they themselves provide a constraint for ocean and habitability models, since the growth of such particles requires moderate salinity, alkaline pH and warm temperatures ($>$363 K) (Hsu et al. 2015; Sekine et al. 2015).

3 Enceladus' Energy Flux

3.1 Introduction

3.1.1 Enceladus' Inputs and Losses

Enceladus has two sources of energy: radiogenic heating from the radioactive decay of heavy elements in its core, and tidal heating due to its eccentric orbit of Saturn. The current day estimate of Enceladus' radiogenic heat is predicted to be $\leq$0.3 GW. Hemingway and Mittal (2019) estimate it to be $<$0.3 GW based on a chondritic radiogenic heating rate of $5\text{x}10^{-12}$ W kg^{-1} (Spohn and Schubert 2003) and a chondritic mass fraction of 0.5. Other studies estimate it to be $\sim$0.3 GW (Schubert et al. 2007; Travis and Schubert 2015), based on chondritic abundances of ^{235}U, ^{238}U, ^{232}Th, and ^{40}K. Either way, this is a lot lower than the 1.8 to 150 GW predicted by tidal heating (Lainey et al. 2020, 2017), and thus tidal heating is expected to be the dominant source of Enceladus' energy.

As previously mentioned, Enceladus and Dione are in a 2:1 mean motion resonance, which means Enceladus orbits Saturn twice, for every one of Dione's orbits. This resonance perturbs Enceladus' orbit, keeping it at a forced eccentricity of 0.0047 (Meyer 2008).

Furthermore, Enceladus is in a synchronous rotation of Saturn (i.e., its spin period and its orbital period are the same, and so the same hemisphere of Enceladus always faces Saturn). As such, Saturn's intense gravitational field deforms Enceladus along the line connecting the centers of the two bodies. This deformation creates a tidal bulge on Enceladus. Since the distance between Saturn and Enceladus is constantly changing (due to the non-zero eccentricity) the size of this tidal bulge is constantly varying too. Enceladus' own interior friction resists this change to its bulge, which results in heating. A more complete description of the complexities of tidal modeling are described in Nimmo et al. (2023, this collection).

In this section we consider how much of this energy Enceladus is able to dissipate as exogenic heat. Specifically, we describe the methods that have been used to constrain this heat flow, and their strengths and limitations.

3.1.2 Passive Thermal Models

In order to understand how much of Enceladus' heat flow is endogenic the exogenic component often needs to be well constrained. This is done through thermal models, which use the thermophysical properties of a surface to predict its passive surface temperature. This is usually achieved by solving the 1-dimensional heat equation:

$$\rho c_p \frac{\partial T(z,t)}{\partial t} = \frac{\partial}{\partial z}\left(\kappa \frac{\partial T(z,t)}{\partial z}\right) \tag{1}$$

Where ρ is the density, c_p is the specific heat capacity, κ is thermal conductivity, T is temperature, t is time and z is regolith depth. The 1-D heat equation can be simplified by writing it in terms of the surface's skin depth (l_s), which is defined as $l_s = \sqrt{\frac{\kappa}{\rho c_p \omega}}$, where ω is the angular rotation of the body. If the depth is now expressed in terms of the skin depth ($Z = \frac{z}{l_s}$) then the 1-D heat equation reduces to:

$$\frac{\partial T(Z,t)}{\partial t} = \omega \frac{\partial T(Z,t)}{\partial Z^2} \tag{2}$$

The upper boundary of these models balances the absorbed solar insolation against infrared emission to space:

$$\kappa \frac{\partial T(z,t)}{\partial z} \,|_{z=0} = \varepsilon \sigma T(0,t)^4 - (1-A)\, F_{\odot} \tag{3}$$

Where $(1-A)\, F_{\odot}$ is the solar heating rate (i.e., the surface energy flux), A is the albedo, $F_{\odot}$ is the incident solar flux, ε is the infrared emissivity, σ is the Stefan–Boltzmann constant, and $T(0,t)$ is surface temperature. This boundary condition can also be rewritten in terms of skin depth:

$$\sqrt{\kappa \rho c_p \omega} \frac{\partial T(Z,t)}{\partial Z} \,|_{z=0} = \varepsilon \sigma T(0,t)^4 - (1-A)\, F_{\odot} \tag{4}$$

Changing the boundary condition into these terms is useful, because all of the physical parameters are now combined into a single term, known as thermal inertia (Γ) which is defined as $\Gamma = \sqrt{\kappa \rho c_p}$. So, the boundary condition can be rewritten as:

$$\Gamma \sqrt{\omega} \frac{\partial T(Z,t)}{\partial Z} \,|_{z=0} = \varepsilon \sigma T(0,t)^4 - (1-A)\, F_{\odot} \tag{5}$$

In order to accurately set the upper boundary condition the albedo, thermal inertia, emissivity and rotation state of the surface must be known. Typically only the rotation state is well constrained, and the uncertainty of the other parameters translates into uncertainty in the surface temperatures predicted.

At the base of a passive model, it is assumed there is no heat flux through the boundary, that is:

$$\Gamma\sqrt{\omega}\frac{\partial T(Z,t)}{\partial Z}\ |_{z=d}=0 \tag{6}$$

This implies the temperature at the boundary is unchanged with both time and location. While we know this is not completely correct (heat is being transported from the relatively warm ocean to the cold outer ice shell), this heat flow is usually much lower than the solar forcing and thus this assumption holds. In order for these conditions to be met the boundary must be set much lower than the seasonal and diurnal skin depths.

Different models parametrize the required variables in different ways. The simplest models assume them to be constant (e.g., Spencer et al. 1989), while some assume specific heat, thermal conductivity and density vary with temperature (e.g., Hayne and Aharonson 2015). The choice of what to assume often depends upon how well the surface properties are known, and how accurately the problem needs to be solved. How such models can be used and constrained are explored in the next sections.

3.1.3 Deriving Enceladus' Surface Temperature

The Cassini spacecraft toured the Saturn system between 2004 and 2017 and provided a wealth of data from its suite of instruments on Enceladus. Cassini's Composite Infrared Spectrometer (CIRS) (Flasar et al. 2004) measured thermal infrared emission from Enceladus and as such provides some of the strongest constraint on Enceladus' heat flow. CIRS is a Fourier Transform Spectrometer (FTS), made of two interferometers that share a single scan mechanism and telescope. Wavenumbers between 10 and 600 cm^{-1} (16.7 to 1000 μm) are detected by two thermopile detectors known as focal plane 1 (FP1), which has a spatial resolution of 3.9 mrad. Higher wavenumbers, between 600 and 1100 cm^{-1} (9.1 to 16.7 μm), are detected by focal plane 3 (FP3). Focal plane 4 (FP4) is sensitive to wavenumbers between 1100 and 1400 cm^{-1} (7.1 to 9.1 μm). FP3 and FP4 both have a row of ten detectors, each of which has a 0.273 by 0.273 mrad field of view. This means FP1 has a spatial resolution $\sim$10 times lower than that of FP3 and FP4, but its wavelength coverage makes it more sensitive to lower temperatures as it covers the peak of the blackbody emission curve for all temperatures cooler than 320 K.

Figure 8 compares the wavelength coverage of CIRS' focal planes to blackbody emission at 30 K, 80 K and 150 K. As the figure shows FP1 is sensitive to the bulk of the emission from cooler temperatures, enabling it to reliably detect temperatures $>\sim$25 K (Howett et al. 2016). However, due to FP3 and FP4's shorter wavelength sensitivity they are only sensitive to warmer temperatures, with FP3 only being reliably sensitive to temperature greater than $\sim$80 K and FP4 to regions even warmer than that (Howett et al. 2019). In fact, on Enceladus FP4 was only sensitive to its warmest surface temperatures: its active tiger stripes. FP3 was sensitive to the tiger stripes and daytime emission, whereas FP1 was sensitive to the tiger stripes, day and nighttime emission. This means that CIRS is well suited to deriving Enceladus' surface temperatures, but a trade has to be made between its sensitivity to temperature and spatial resolution.

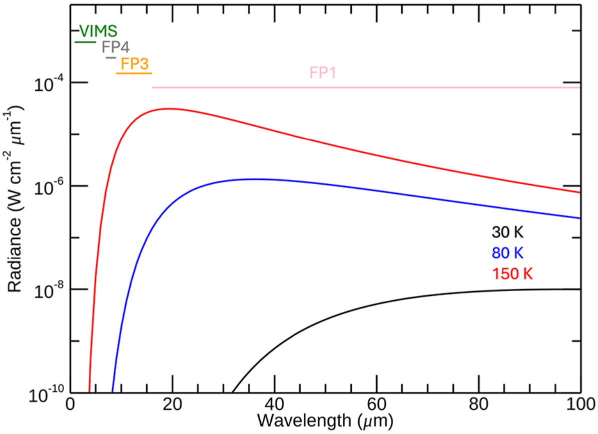

Fig. 8 A comparison of the radiance from blackbody emission at 30 K (black), 80 K (blue) and 150 K (red) to the wavelength range of the CIRS focal planes 1 (FP1, pink), 3 (FP3, orange) and 4 (FP4, grey), and the VIMS instrument (green)

The IR channel (0.85 to 5.1 μm) in Cassini's VIMS instrument enabled VIMS to constrain Enceladus' tiger stripe emission and surface properties (Filacchione et al. 2022; Goguen et al. 2013). Filacchione et al. (2022) used the position of the 3.6 μm continuum peak as a proxy for temperature, deriving daytime surface temperature maps for all of Saturn's large satellites, including Enceladus. VIMS is only sensitive to warm (>88 K) surface temperatures (Fig. 8), so the coverage of these maps is restricted to Enceladus' equatorial and mid-latitudes. Goguen et al. (2013) used a unique set of VIMS observations to constrain Enceladus' SPT surface temperature. During an unusually low (74 km) altitude pass of Enceladus VIMS took spectra every 0.025 seconds. The spatial resolution of each observation was 38 m, and 214 m along track (driven primarily by Cassini's 7.5 km/s velocity). Analysis of the 3 to 5 μm spectra provided a surface temperature constraint of Baghdad Sulcus of 197 ± 20 K over a width of 9 m.

3.2 Enceladus' Current Heat Flow

3.2.1 Thermal Measurements

The heat flow from Enceladus' South Polar Terrain (SPT) has been constrained using a variety of methods. Each one has its advantages and disadvantages, and none are without some large assumptions. The first constraint placed on the SPT's heat flow used an SPT FP3 observation along with a thermal inertia of 20 MKS graybody fit to constrain the emission to be 133 ± 12 K over 345^{+320}_{-160} km^2, to give a total estimate of Enceladus' endogenic emission of 5.8 ± 1.9 GW (Spencer et al. 2006). This study did not include any kinetic and latent heat of the plume, and (since they used FP3) were not sensitive to any low-temperature (<80 K) endogenic emission.

To convert this total endogenic power into a power per unit area an SPT bound needs to be assumed. To show the effect of the assumed area we use two regions, the first a great circle at 68°S, chosen because it encompasses the entire tiger stripe region (Fig. 9). However, this bound also includes a lot of non-stripe region, and so may lead to an underestimate of the emission. Thus, a second bound is also used, this one is formed by joining four corner points by great circles; the points are located at: 100°W/68°S, 170°W/°68S, 250°W/°70S and 345°W/°70S (Fig. 9). The circular bound provides an SPT estimate of 29,051 km^2; the rectangular bound an estimate of 16,655 km^2. Using these bounds the heat flow of Spencer et al. (2006) ranges from 200 ± 65 mW m^{-2} to 348 ± 114 mW m^{-2}.

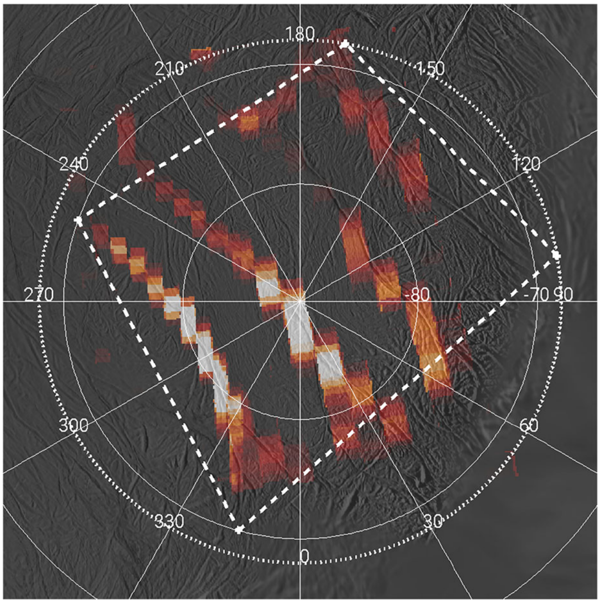

Fig. 9 Radiated 600-1100 cm^{-1} brightness of Enceladus' four tiger stripes, as determined from Cassini/CIRS FP3 using observations obtained on 12th March 2008 (Howett et al. 2011). Overlaid (dotted and dashed lines) are two potential SPT bounds. The dashed line is the most conservative estimate of SPT area only including the active tiger stripes. It assumes the SPT is bounded by great circles joining four points at: 100°W, 170°W, 250°W and 345°W/68°S, 68°S, 70°S and 70°S, providing an SPT area of 16,655 km^2. The dotted line defines the SPT as all terrain within 68°S, providing a larger SPT area of 29,051 km^2. Base map is PIA08417

To determine how much endogenic emission was coming from both low-temperature and high-temperature endogenic emission another study analyzed two FP1 stares of Enceladus' SPT (Howett et al. 2011). The stares, both taken in 2008, covered all of the SPT and a little of the surrounding terrain. However, since these observations were sensitive to cooler temperatures they were sensitive to both the endogenic and passive emission. So, in order to determine the endogenic component of the stares the passive surface emission had to be predicted. In order for the passive emission to be accurately predicted Enceladus' surface properties (albedo, thermal inertia) have to be well constrained (see Sect. 3.1.2). Since they are not well constrained, a range of reasonable values were adopted to test the sensitivity of the predicted power to them. An albedo (0.80) and surface thermal inertia (27 MKS) were assumed because they are the thermophysical properties derived closest to the SPT (in a band between 60°S to 50°S by Howett et al. 2010). Three thermal inertia scenarios were tested: 27 MKS at all depths, 27 MKS from the surface to 1 cm and then increasing to 100 MKS or 1000 MKS.

The FP1 response is a 2D Gaussian with a FWHM of 2.42 mrads (Flasar et al. 2004). Thus, FP1 is also sensitive to the spatial distribution of the endogenic emission across the SPT. To test this sensitivity to the distribution of endogenic emission three scenarios were tested: assuming the tiger stripes are the sole emission source and that the emission is uniform (scenario #1) or varying along the stripe according to FP3 results (as shown in Fig. 9) (scenario #2). The final scenario (#3) assumes all of the emission comes within 10% of the field of view (FOV). Scenario #3 was not expected to be realistic, but rather provided a lower limit to the endogenic emission.

These three thermal inertia and emission scenarios, along with the two FP1 observations, provided the 18 estimates of the SPT's endogenic emission shown in Table 3. As the Table shows for the most likely emission scenarios (i.e., #1 and #2) the predicted endogenic emission varied between 12.9 and 19.3 GW, which led to the final estimate of 15.8 ± 3.1 GW. This estimate did not include latent heat, which could add ~0.7 GW more to the total (Inger-

Table 3 Variation in derived endogenic emission assuming an albedo of 0.80 and three different subsurface conditions. See text for more details. From Howett et al. (2011)

Assumed conditions for thermal model	Endogenic power for Rev 61 uniform spatial distribution (GW)	Endogenic power for Rev 61 FP3-like spatial distribution (GW)	Endogenic power for Rev 61 central spatial distribution (GW)	Endogenic power for Rev 91 uniform spatial distribution (GW)	Endogenic power for Rev 91 FP3-like spatial distribution (GW)	Endogenic power for Rev 91 central spatial distribution (GW)
Scenario 1	16.6	13.8	8.2	19.3	16.9	11.9
Scenario 2	15.5	12.9	7.6	17.2	15.0	10.6
Scenario 3	16.6	13.8	8.1	16.6	14.5	10.2

soll and Pankine 2010). This translates to a heat flow between 543 ± 107 to 949 ± 186 mW^{-2} depending upon the SPT area assumed.

This ∼16 GW total heat flow estimate was ∼10 GW greater than the previous estimate, and at the time posed a problem to the scientific community. How could Enceladus be producing this much emission when the orbital evolution models at the time predict equilibrium rates about an order of magnitude lower than this (Meyer and Wisdom 2007)? Periodic release and a varying dissipation factor Q of Saturn were put forward as possible explanations. Since then, estimates of Q have evolved, and current estimates predict the equilibrium heating rate of Enceladus to be 50 to 150 GW (Lainey et al. 2020, 2017; also see Lainey et al. 2025 and Nimmo et al. 2023, this collection), well above the 15.8 GW measured in this study.

The results of Howett et al. (2011) are heavily model dependent, and do not resolve the heat flow from individual stripes themselves. So, a follow-on study was developed to combine FP1, FP3 and FP4 results to better understand the spatial variation of the endogenic emission (Howett et al. 2013; Spencer et al. 2018). It was assumed the emission is constant with time, and so observations taken at different epochs could be used to constrain it. It was also assumed that the emission had to be able to explain the observations at all wavelengths, so a single model could be used to explain emission across FP1, FP3 and FP4 wavelength ranges.

Two sets of observations were used: an FP3 and FP4 scan of the entire SPT taken in March 2008, and an FP1 scan across Damascus, Baghdad and Cairo taken in August 2010 (Fig. 10a and 10b). The first step was to divide the CIRS emission into wavelength bins, to ensure that different parts of the surface's blackbody emission were well characterized. The FP1 radiances were integrated over bins from 25-83 μm, and 83-200 μm. This was repeated for three wavelength regions in FP3: 9.5 to 11.1 μm, 11.1 to 13.3 μm and 13.3 to 16.7 μm, and between 7.7 and 9.1 μm for FP4.

A model of the width and magnitude of the low- and high-temperature endogenic emission along each of the stripes was then developed (Fig. 10e). Interestingly the initial model was unable to fit the emission from one side of Baghdad sulci and required an additional fracture to be added to provide an adequate fit (Figs. 10c and 10d). There was no previous indication from optical maps or other sources that this fracture was active. The lack of activity detection in optical maps is not unique. The warm subsurface regions observed by synthetic aperture radar (SAR) observations (discussed further below) also did not have other indications of activity (Le Gall et al. 2017).

The endogenic modelling results showed a high-temperature component of 3.1 GW, a low temperature component of 1.3 GW, which provided a total of 4.9 GW (including 0.5 GW

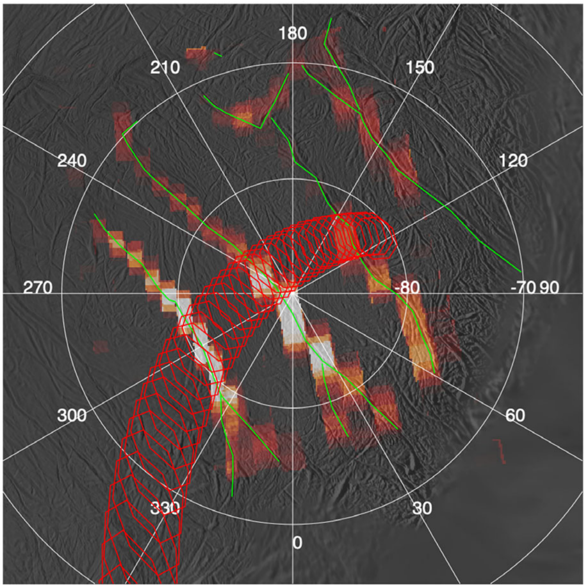

(a) - August 2010 FP1 scan across Damascus, Baghdad and Cairo is shown in red. The locations of the tiger stripes are shown in green. Overlaid on the March 2008 FP3 base map (Figure 4).

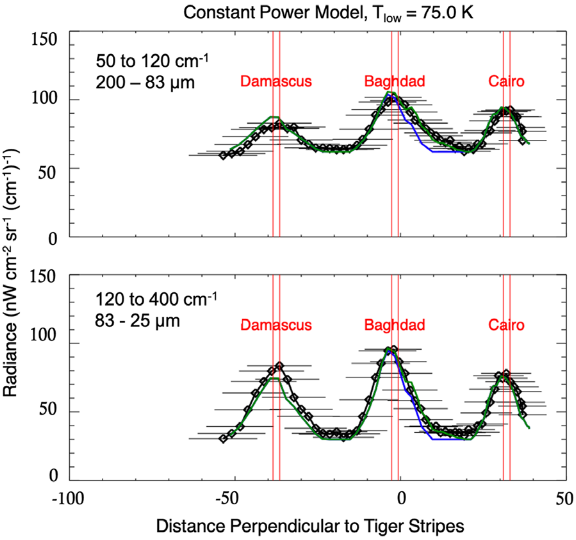

(b) Integrated FP1 radiance over two wavelength bands, 200-83 μm (top) and 83-25 μm (bottom) are shown by the black points. The black horizontal lines show the extent of each observation's FOV. The red vertical lines show the location of each of the three tiger stripes in the scan and are labeled accordingly. The model fits to these data are shown without (blue) and with (green) the additional Baghdad branch (position shown in (c)) included.

Fig. 10 The data (a and b) used to fit the temperature and emission width across the various tiger stripe fractures (c and d). The results from the fit are shown in (e). From Howett et al. (2013) and Spencer et al. (2018)

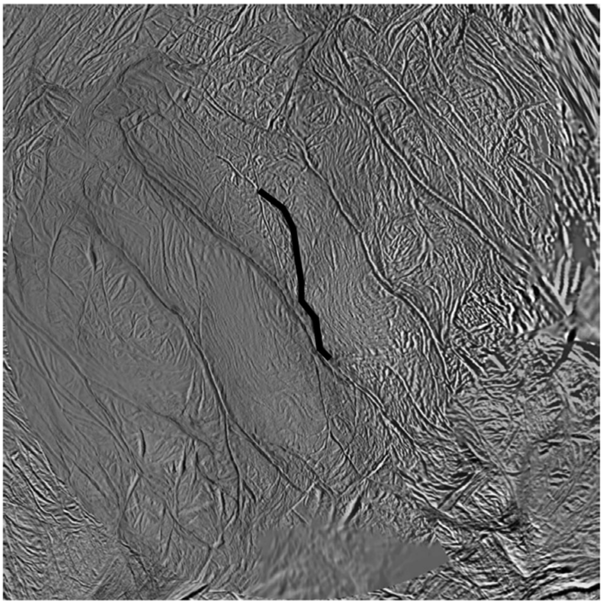

(c) Location of the additional warm stripe required to produce the model fit shown in (a).

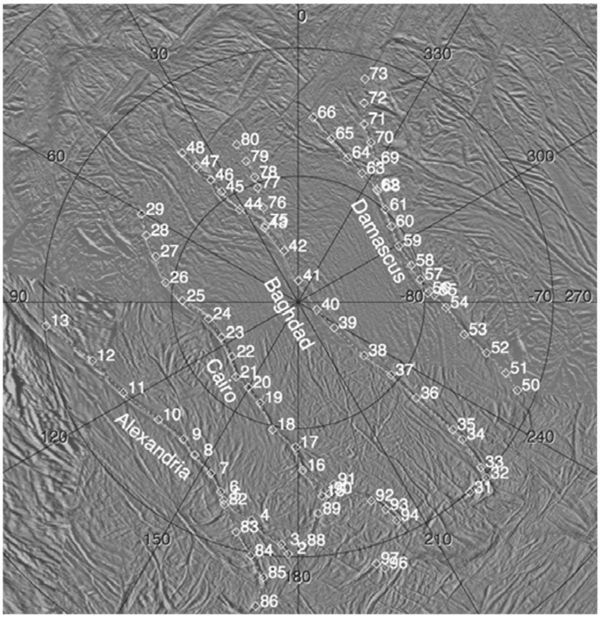

(d) The positions of the modeled emission temperatures and widths.

Fig. 10 (*Continued*)

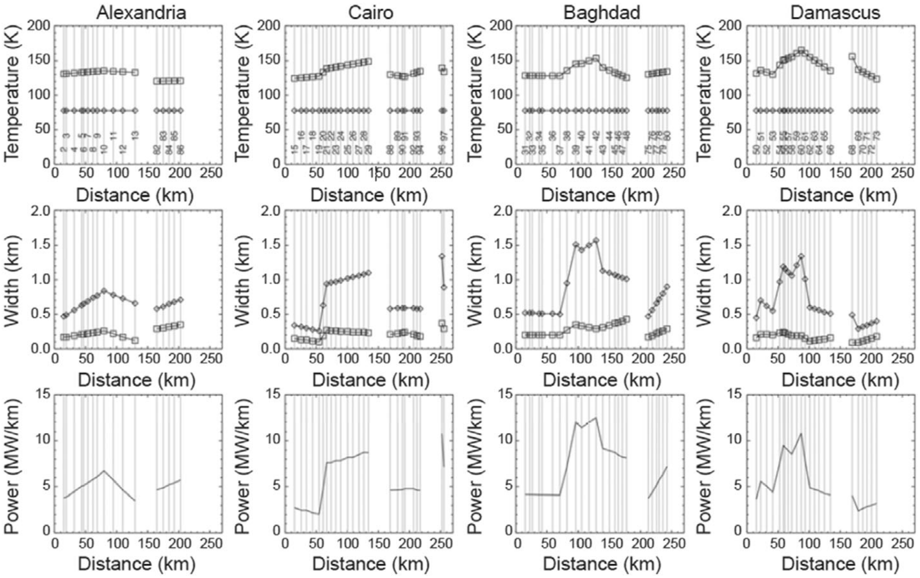

(e) Model emission widths and temperatures, and their corresponding power per unit length at each position indicated in the top figure (the same numbering scheme is used in the temperature plots as shown in the top figure). The points at the line were calculated, and the intermediate points were interpolated.

Fig. 10 (*Continued*)

of latent heat), or 169 to 294 mW m^{-2}. This method does not include any emission from between the stripes. Emission from any other small fractures (if more are active) were also not included. So, this method provided a robust solution for the lower bound of Enceladus' endogenic emission but not its total emission.

New work on modeling the interstitial (i.e., between stripe) regions of Enceladus is ongoing. Howett et al. (2022) (Fig. 11) showed the results of modeling a high-spatial resolution FP1 scan that cut across Damascus, Baghdad and Cairo sulci. These observations put the FP1 FOV in between the stripes, and so could measure their temperature directly. Since these are FP1 observations the passive emission component needed to be removed, but this time it was constrained using observations from the same scan that were taken close to the tiger stripes but outside the active regions. This requires the feasible assumption that the thermophysical properties inside and outside the stripes were similar, and if the model could fit the surface temperatures close to the stripes, then it would follow that it was modeling the passive temperatures inside the stripes. Depending on the passive model assumed, this work predicts the interstitial heat flow alone to be between 2.9 ± 0.5 GW and 4.0 ± 0.4 GW. This translates to an interstitial heating rate of (99 ± 17 to 174 ± 30 mW m^{-2}) and (138 ± 14 to 240 ± 24 mW m^{-2}).

Table 4 compares the results of the various studies that have modeled Enceladus' endogenic emission. It highlights the advantages and disadvantages of each study and shows that obtaining the "true" value of Enceladus' endogenic emission remains elusive. Arguably the most robust measurement of the stripe emission comes from Spencer et al. (2018), which sets a lower bound of 4.9 GW. If this is combined with the lowest bound of the between-stripe emission (2.4 GW), then the current best estimate of Enceladus' endogenic emission is

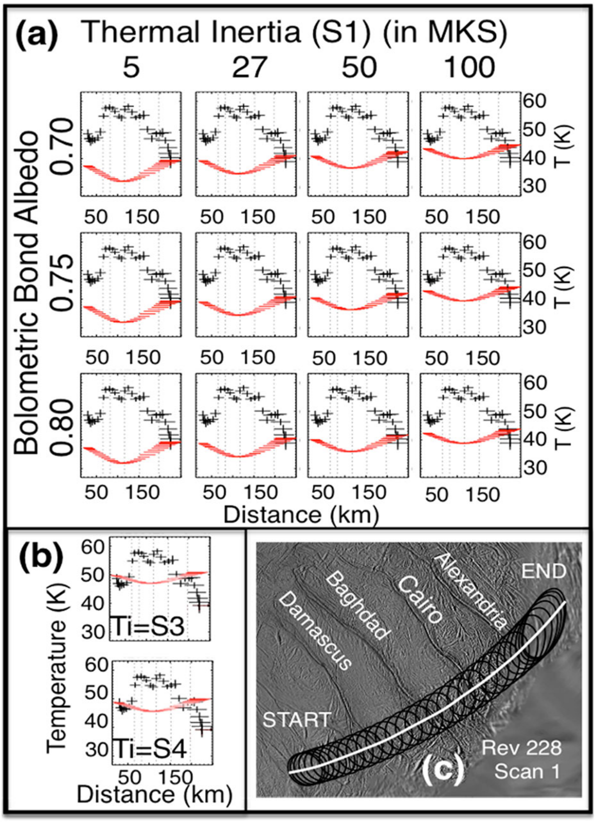

Fig. 11 A comparison of passive modeled and CIRS derived surface temperatures, showing none of the models fit the interstitial temperatures. (a) Temperature derived from Rev 228 (Dec 2015) CIRS data (black) and those predicted by passive thermal models (red) for a range of albedo (rows) and thermal inertia (columns). In all models the thermal inertia is constant with depth (S1). "Distance" is calculated as the distance from the start of the white line in (c) to where the line intersects the nearest and furthest points of the field of view. Dotted lines indicate where the line crosses the tiger stripes, from left to right: Damascus (both branches), Baghdad, Cairo and Alexandria. (b) Same as the top plot, but for seasonal models with an albedo 0.80 and a thermal inertia profile that changes with depth. (c) Footprints of the CIRS FP1 field of view (black). Tiger stripe names are indicated. Figure from Howett et al. (2022)

>7.3 GW (>251 mW m^{-2}). Current estimates of non-SPT emission are lacking, but there is preliminary evidence from CIRS of endogenic emission from Enceladus' north polar region (Miles et al. 2022).

3.2.2 Inference from Geology

A finite-element model was used to predict the heat flow required to form the periodic low-slope features found across Sarandib and Diyar Planitia, close to Enceladus' equator (Bland et al. 2007). The study used photoclinometry to show these regions have a periodic wavelength of 3 to 4 km and amplitudes between 100 and 400 m. Comparisons of the finite-element model to the photoclinometry results to predict a heat flow between 110 and 220 mW m^{-2} at the time of their formation. This suggests a strong localized heating source was present at the time of their formation, which is estimated to be 50 Ma to >3 Ga depending on the adopted model of impactor flux (Kirchoff and Schenk 2010; Porco et al. 2006a). Similar finite-element modeling work was also conducted on relaxed craters in Enceladus' equatorial and mid-latitude regions (North and East of Hamah Sulci). The results showed that heat flows of ∼150 mW m^{-2} were required to explain their relaxation, and their shape was best explained by short period of intense heating (Bland et al. 2012).

Models of flexural deformation at Enceladus's Harran Sulci (which covers equatorial to mid-northern latitudes) were used to constrain the likely heat flux at its formation (Giese et al. 2008). Depending upon the assumed surface porosity heat flows between 45 mW m^{-2}

Table 4 A comparison of the heat-flows predicted for Enceladus, both inside and outside its SPT. The heat flow in $\mathrm{mW\,m^{-2}}$ is given assuming the SPT is the region south of 68°S. The lower limit given by Howett et al. (2022) plus Spencer et al. (2018) combines the lowest bound of Howett et al. (2022) (i.e., 2.9-0.5) to that of Spencer et al. (2018). Light grey indicates desired answered, while dark grey indicates solutions that require additional consideration

SPT studies

Source	Region	Power ($\mathrm{mW\,m^{-2}}$) (Assuming SPT is inside 68°S)	Power (GW)	Include all SPT emission?	Need to remove passive?	Include high- and low-temperature?
Spencer et al. (2006)	SPT	200 ± 65	5.8 ± 1.9	Yes	No	No
Howett et al. (2011)	SPT	543 ± 107	15.8 ± 3.1	Yes	Yes	Yes
Spencer et al. (2018)	SPT	>169	>4.9	No (just tiger stripes)	No	Yes
Howett et al. (2022)	SPT	99 ± 17 to 138 ± 14	2.9 ± 0.5 GW to 4.0 ± 0.4 GW	No (just interstitial regions)	Yes	Yes
Spencer et al. (2018) + Howett et al. (2022)	SPT	>251	> 7.3	Yes	Yes	Yes

Non-SPT studies

Source	Region	Power ($\mathrm{mW\,m^{-2}}$)	Notes
Le Gall et al. (2017)	∼10 km north of the tiger stripes	500	Radar thermal anomaly 10 s of cm below surface (nothing in thermal emission)
Bland et al. (2007)	Sarandib and Diyar Planitia (equatorial)	110 to 220	Heat flow required at formation (50 Ma to >3 Ga)
Bland et al. (2012)	North and East of Hamah Sulci (equatorial and mid-northern latitudes)	150	Heat flow required at formation (<2 Ga)
Giese et al. (2008)	Harran Sulci (equatorial and mid-northern latitudes)	45 to 270	Heat flow required during formation ($0.45^{+1.1}_{-0.3}$ to $3.5^{+0.1}_{-0.4}$ Ga)

to 270 $\mathrm{mW\,m^{-2}}$ are required to explain the observed topography, which is believed to be formed between $0.45^{+1.1}_{-0.3}$ and $3.5^{+0.1}_{-0.4}$ Ga (depending on whether a comet-like impactor chronology, or an asteroid-like one is assumed).

3.2.3 Inference from Radar

On 6th November 2011 Cassini's RADAR instrument observed Enceladus' south polar region from 500 km above the surface. The microwave radiometry (2.2 cm) results, which are sensitive to ∼10 s of centimeters beneath Enceladus' surface, showed a subsurface with a warm, thermally anomalous region (Le Gall et al. 2017). The location of this thermal anomaly was ∼10 km north of the tiger stripes and was not spatially related to any sulci similar to the tiger stripes. The temperature varied from $32^{+0.6}_{-2.6}$ K to $60^{+1.2}_{-4.8}$ K, while these are cold they are above the expected passive surface temperature in this region. The total difference was estimated to require a heat flow of $\sim$500 mW m^{-2}. Warmer surface temperatures were not recorded in this region by CIRS. One explanation is that the deeper radar observations sensed a dormant or "dying" sulcus (i.e., one that is no longer active and is slowly losing its excess heat). This sulcus is too cold to be distinguishable from the passive background at the surface (or is being masked from the surface by an insulating layer). Thus, it is feasible that there are other previously active sulci across Enceladus, but they remain undiscovered.

Further analysis of 2.2 cm disk-integrated radar observations of Enceladus shows the lower limit of its emissivity to be larger than expected (Le Gall et al. 2023). One possible explanation for this is that their initial assumption of no endogenic emission is incorrect. This would support the preliminary conclusion from CIRS (Miles et al. 2022) that actually Enceladus' endogenic emission is not confined to the SPT.

3.2.4 Conductive Heat Loss Estimates

Heat from Enceladus' relatively warm subsurface ocean is expected to conduct through its ice shell, eventually being radiated to space. The amount of heat lost depends upon the thickness of Enceladus' ice shell, which has been estimated using geodetic observations from Cassini data (Hemingway and Mittal 2019; Iess et al. 2015; Čadek et al. 2016; Schenk and McKinnon 2009; Thomas et al. 2016; Park et al. 2024). Differences in the ice shell thickness assumed lead to variations in the predicted conductive heat loss estimate for Enceladus. Hemingway and Mittal (2019) use a shell thickness model to predict losses between 20 and 35 GW, while Čadek et al. (2016) and Park et al. (2024) estimate values between 25 and 30 GW, and 18 and 28 GW respectively. These may be compare with equilibrium tidal heating rates between 1.8 and 150 GW depending on the assumptions made (Rhoden et al. 2015; Lainey et al. 2017; Nimmo et al. 2023).

4 What Further Observations Are Needed?

Cassini's amazing tour taught us a great deal about Enceladus' mass loss, but of course many questions remain. Due to Enceladus' small size, proximity to Saturn, and activity located at the poles (which are out of sight from Earth) future observations to solve these questions mostly require a spacecraft to return to the Saturn system. In fact, many of the outstanding questions either need high-spatial resolution coverage, or observations taken at regular time intervals. Both of these types of observation would be well served by a mission that was in orbit around Enceladus (and not Saturn). The following suggestions are not given in a priority order. Rather we defer to NASA's decadal survey (National Academies 2022) as a far more comprehensive study of the priories of Enceladus' exploration. We simply note that with Enceladus listed as a suggested target for New Frontiers 5 and 6, and an Enceladus Orbilander being the second-highest priority Flagship mission, future exploration of Enceladus is a very real possibility.

Flying a high-resolution mass spectrometer that is sensitive to heavy ($>$50 u) molecules through Enceladus' plumes would enable many of the outstanding composition questions to be resolved. For example, on the abundance of high-mass (e.g., C_2 and C_3 carbon) species. It would also enable the composition of lower-mass species to be differentiated (e.g., what are the species contributing to the 28 u feature)?

A high-spatial ($<$100 m) resolution thermal instrument could accurately determine how the thermal emission varies along and between the tiger stripes. This would enable the connection between plume emission and latent heat release to be studied and might determine whether the surface heating from latent heat release is higher over the jets. Since jets have denser plume emission, there is more material available to freeze out onto crack walls to release latent heat.

Thermal observations of the SPT by an instrument capable of detecting polar winter temperatures ($\sim$30 K) and resolving the regions between the stripes would enable the conduction of heat from the fissures to be studied. This would address questions on the heat flow through the ice shell, such as how efficient is the surface conduction, and how far away from the stripes is heated by them? If such an instrument were able to measure the global surface temperature, then small regions of undiscovered activity could be searched for, and a constraint put on Enceladus' global heat flow.

Observations that determine both the spatial distribution and temporal variability of the solid and vapor plume sources are required to constrain Enceladus sub-surface plumbing. The constraint on their spatial variation would enable questions about the source of the solid/vapor to be determined. For example, it could answer whether solids are ejected by curtains or jets (or both)? Do some sources only emit one (or the other)? These observations would be even more powerful if they were taken in addition to the thermal measurements because then the connection between the heat, solid and vapor sources could be determined.

A study of the solid and vapor particle's temporal variability with short- and long-term coverage would enable questions on their forcings to be determined. For example, are vapor and solids modulated by tides in the same way? Fully understanding their short and long-term variability (rather than patchy coverage) would better constrain the time lag between the tidal forcings and the plume's response, perhaps even addressing the question of why the plumes do not cease emission during periapsis (when the fractures should be closed)? Such observations made over $\sim$decadal timescales could constrain the length and magnitude of global changes in plume brightness (like those seen at the end of the Cassini mission).

5 Conclusions

The Cassini mission revealed not only the presence of Enceladus' activity but allowed it to be studied in detail. Observations from the mission reveled surface warming around four fractures within Enceladus' SPT, and a plume that erupts from them. The energy and mass loss from both the surface warming and plumes were constrained by both in situ and remote observations.

The greatest source ($\sim$80%) of the mass loss via the plumes is from vapor, with between 100 and 250 kg/s being lost (see references in Table 2). The vapor is mostly water ice, with some carbon dioxide, ammonia, molecular hydrogen, and trace species, expected to come from evaporating ocean water. The loss of molecular hydrogen was specifically studied, as it provides support that Enceladus has active hydrothermal processes (Waite et al. 2017). Its current loss rate is estimated to be between 0.002 and 0.01 kg/s, so a very small fraction of the total vapor – but an important one!

This vapor almost always escapes Enceladus into space, since its low mass allows it to be more easily accelerated to speeds above Enceladus' escape velocity (Hansen et al. 2006). The bulk vapor mass loss rate seems to be approximately constant with time (albeit with individual jets increasing and reducing their specific vapor loss (Hansen et al. 2017; Teolis et al. 2017). However, the vapor has notable spatial variation, with heavier components (CO_2) having a smaller lateral spread than the lighter ones (H_2, H_2O) (Perry et al. 2015; Yeoh et al. 2015). So, all of this combines to Enceladus consistently losing a lot (100 to 250 kg/s) of (predominantly water) mass into space.

Solid particles provide the next highest mass flux (10%), with between 3 and 65 kg/s being ejected into space. However, these heavier particles are less able to reach Enceladus' escape velocity, and so between 90 and 95% will fall back onto Enceladus' surface (Schmidt et al. 2008). Unlike the vapor the mass-flux of these particles varies both temporally and spatially. The plumes are brightest (highest mass-flux) just after apoapsis (MA=180°) at MA=200°. There is also a secondary double-peaked maximum at MA of 25° and 60° (Hedman et al. 2013; Nimmo et al. 2014; Ingersoll et al. 2020). If this wasn't enough the total plume brightness also changes with the years (Ingersoll et al. 2020). Tidal stresses on Enceladus' surface are believed to be the cause of the orbital-length variation, with the plumes decreasing in output when the fractures are squeezed closed when the surface is under compression at apoapsis, and increasing when the fractures are pulled apart when the surface is under tension at periapsis (e.g., (Nimmo et al. 2014)). Tides are also thought to explain the multi-year changes, with the surface changing in response to Enceladus and Dione's 4- and 11-year tidal cycle (Porco et al. 2018).

The spatial variation of plume particles follows a more complex pattern than that of the vapor, linked to its composition. Broadly the plume particles can be separated into three types (Postberg et al. 2011). Type 1 particles make up the bulk of the plume (65%) and are small particles mostly made of pure water ice. Type 2 is the next most abundant (25% by mass) and are approximately speaking a larger version of Type 1, but with some additional silicates, salts and varying organics. Arguably the most interesting is Type 3 particles, which have the lowest abundance (∼10% by mass) but have a very different composition from their counterparts, most notably containing silicon. They are believed to be frozen droplets of Enceladus' ocean, and the presence of salts and silicon imply that the ocean must be in direct contact with the core. They allow the composition of the ocean to be sampled, without disturbing it. This means that while the solid particles might not be the major source of mass flux, what is being lost provides unparalleled insight into Enceladus' interior (Postberg et al. 2011). Finally, nanograins and ions are estimated to have a mass flux of 15-65 kg/s and 5.6 kg/s respectively, roughly equivalent to that of the plume particles (Dong et al. 2015; Kempf et al. 2018). However, unlike the particles these charges species are small and so likely to escape - eventually ending up in Saturn's magnetosphere.

Our understanding of Enceladus' mass flux has evolved with observations and models. These current estimates provide a likely total mass flux of ∼240 kg/s, meaning Enceladus could lose 7 billion kilograms of material every Earth year. Using the best estimate of the mass and composition of Enceladus' ocean, means activity at its current level could be sustained up to ∼1.5 billon Earth years. The loss of molecular hydrogen constrains this further, limiting the activity to less than one million Earth years unless resupplied (e.g. by serpentinization).

A range of studies, using different instruments and/or models, show Enceladus to be a place of high surface heat flows, both now and in the past. Each of the studies tells a different part of the story, some setting bounds, and many investigating different epochs and regions of Enceladus. Despite this work it is difficult to know what Enceladus' current heat flow really is. The highest heat flows are observed in its South Polar Terrain, and the different methods used to constrain the SPT heat flow have provided a lower limit of tiger stripe emission of 169 $\mathrm{mW\,m^{-2}}$ (∼4.9 GW, Spencer et al. 2018). This can be reasonably extended to >251 $\mathrm{mW\,m^{-2}}$ (>7.3 GW) by including the lowest bound of our best estimate of between-stripe emission (Howett et al. 2022) and the least conservative bound on the SPT area (i.e., all the regions south of 68°S). However, Enceladus SPT is only a small fraction of its total area, and so despite its high surface heat flows it alone only tells part of the story. The challenge remains in separating out the lower endogenic heat flows from the passive emission across the rest of Enceladus. This is particularly difficult in regions where it small relative to the passive emission - like the warmer equatorial and mid-latitude regions. Tentative evidence shows that this could be done by global radar studies (Le Gall et al. 2023) and in the considerably colder thermal regime of polar winter (Miles et al. 2022).

Studies of Enceladus' geology show that high heat flows are not restricted to our current epoch, but rather have existed across Enceladus for billions of years. These studies consider the conditions required either for formation, or to enable changes post-formation. The results imply that heat flows between $\sim$45 to 270 $\mathrm{mW\,m^{-2}}$ were required for multiple regions across Enceladus' equatorial and mid-northern latitudes to form (Bland et al. 2007; Giese et al. 2008), which are comparable with the current SPT heat flow estimates. Age estimates using cratering fluxes put these formation events between $\sim$0.42 Ga and $>$3 Ga ago. These heat flows are consistent with the those required to form the relaxed craters seen across Enceladus' equatorial regions (110 to 200 $\mathrm{mW\,m^{-2}}$), which are likely to have occurred within the last 2 Ga (Bland et al. 2012). Evidence of these ancient heat flows may still be present deep in Enceladus' surface, still detectable to long ($>$cm) wavelength instruments that probe deeper into Enceladus' surface than thermal ones. One such region was discovered $\sim$10 km north of the SPT by 2.2 cm radar, a thermally anomalous region with an inferred heat flow of 500 $\mathrm{mW\,m^{-2}}$ (but nothing detectable in surface thermal emission) (Le Gall et al. 2017).

Enceladus is likely to have experienced high heat flows throughout its evolution. However, a final constraint on its current heat flow, both inside and outside of the SPT is lacking. We do not even know how common deep thermal anomalies are! While investigations into the wealth of data returned by the Cassini mission may provide further answers it is likely that additional missions are required to truly answer these questions. A mission that provides long-baseline thermal coverage of Enceladus at consistently high spatial resolutions, throughout both Enceladus' diurnal and seasonal cycles, would constrain its passive emission. This would enable Enceladus' non-SPT endogenic heat flows to be constrained, especially in regions of cold winter darkness where the passive component is minimized. Radar and sub-mm measurements would enable Enceladus' deeper sub-surface to be probed, enabling a picture to be constructed of the global heat flow from deep ancient thermally anomalous regions. These could then be used to finally constrain how Enceladus, and the Saturn-system as a whole, has evolved and what the future has in store.

Funding Information This work was partially funded by ISSI, NASA CDAP 80NSSC20K0477 and NNN12AA01C.

Declarations

Competing Interests The authors have no competing interests to declare that are relevant to the content of this article. CH is a Guest Editor of the collection but was not involved in the peer review process of this article.

References

Ames F, Ferreira D, Czaja A, Masters A (2025) Ocean stratification impedes particulate transport to the plumes of Enceladus. Commun Earth Environ 6:63. https://doi.org/10.1038/s43247-025-02036-3

Berne A, Simons M, Keane JT, Leonard EJ, Park RS (2024) Jet activity on Enceladus linked to tidally driven strike-slip motion along tiger stripes. Nat Geosci 17:385–391. https://doi.org/10.1038/s41561-024-01418-0

Bland MT, Beyer RA, Showman AP (2007) Unstable extension of Enceladus' lithosphere. Icarus 192:92–105. https://doi.org/10.1016/j.icarus.2007.06.011

Bland MT, Singer KN, McKinnon WB, Schenk PM (2012) Enceladus' extreme heat flux as revealed by its relaxed craters. Geophys Res Lett 39:L17204. https://doi.org/10.1029/2012GL052736

Brown RH, Kirk RL (1994) Coupling of volatile transport and internal heat flow on Triton. J Geophys Res Planets 99:1965–1981. https://doi.org/10.1029/93JE02618

Brown RH, Baines KH, Bellucci G, Bibring J-P, Buratti BJ, Capaccioni F, Cerroni P, Clark RN, Coradini A, Cruikshank DP, Drossart P, Formisano V, Jaumann R, Langevin Y, Matson DL, Mccord TB, Mennella V, Miller E, Nelson RM, Nicholson PD, Sotin C (2004) The Cassini Visual and Infrared Mapping Spectrometer (VIMS) investigation. Space Sci Rev 115:111–168. https://doi.org/10.1007/s11214-004-1453-x

Brown RH, Clark RN, Buratti BJ, Cruikshank DP, Barnes JW, Mastrapa RME, Bauer J, Newman S, Momary T, Baines KH, Bellucci G, Capaccioni F, Cerroni P, Combes M, Coradini A, Drossart P, Formisano V, Jaumann R, Langavin Y, Matson DL, McCord TB, Nelson RM, Nicholson PD, Sicardy B, Sotin C (2006) Composition and physical properties of Enceladus' surface. Science 1979(311):1425–1428. https://doi.org/10.1126/science.1121031

Čadek O, Tobie G, Van Hoolst T, Massé M, Choblet G, Lefèvre A, Mitri G, Baland R-M, Běhounková M, Bourgeois O, Trinh A (2016) Enceladus's internal ocean and ice shell constrained from Cassini gravity, shape, and libration data. Geophys Res Lett 43:5653–5660. https://doi.org/10.1002/2016GL068634

Coates WA, Lewis GR, Jones GH, Young DT, Crary FJ, Waite JH, Johnson RE, Hill TW, Sittler EC Jr (2010b) Negative ions at Titan and Enceladus: recent results. Faraday Discuss 147:293. https://doi.org/10.1039/c004700g

Coates JGH, Lewis GR, Wellbrock A, Young DT, Crary FJ, Johnson RE, Cassidy TA, Hill TW (2010a) Negative ions in the Enceladus plume. Icarus 206:618–622. https://doi.org/10.1016/j.icarus.2009.07.013

Coates AJ, Wellbrock A, Jones GH, Waite JH, Schippers P, Thomsen MF, Arridge CS, Tokar RL (2013) Photoelectrons in the Enceladus plume. J Geophys Res Space Phys 118:5099–5108. https://doi.org/10.1002/jgra.50495

Cooper JF, Cooper PD, Sittler EC, Sturner SJ, Rymer AM (2009) Old faithful model for radiolytic gas-driven cryovolcanism at Enceladus. Planet Space Sci 57:1607–1620. https://doi.org/10.1016/j.pss.2009.08.002

Cravens TE, Ozak N, Richard MS, Campbell ME, Robertson IP, Perry M, Rymer AM (2011) Electron energetics in the Enceladus torus. J Geophys Res Space Phys 116:A09205. https://doi.org/10.1029/2011JA016498

Croft S, Kargel J, Kirk RL, Moore J, Schenk P, Strom R (1995) The geology of Triton. In: Cruikshank DP (ed) Neptune and Triton. The University of Arizona Press, Tucson, pp 879–947

Dhingra D, Hedman MM, Clark RN, Nicholson PD (2017) Spatially resolved near infrared observations of Enceladus' tiger stripe eruptions from Cassini VIMS. Icarus 292:1–12. https://doi.org/10.1016/j.icarus.2017.03.002

Dong Y, Hill TW, Ye S-Y (2015) Characteristics of ice grains in the Enceladus plume from Cassini observations. J Geophys Res Space Phys 120:915–937. https://doi.org/10.1002/2014JA020288

Esposito LW, Barth CA, Colwell JE, Lawrence GM, McClintock WE, Stewart AIF, Keller HU, Korth A, Lauche H, Festou MC, Lane AL, Hansen CJ, Maki JN, West RA, Jahn H, Reulke R, Warlich K, Shemansky DE, Yung YL (2004) The Cassini ultraviolet imaging spectrograph investigation. Space Sci Rev 115:299–361. https://doi.org/10.1007/s11214-004-1455-8

Fagents S (2000) Cryomagmatic mechanisms for the formation of rhadamanthys linea, triple band margins, and other low-albedo features on Europa. Icarus 144:54–88. https://doi.org/10.1006/icar.1999.6254

Fagents SA (2003) Considerations for effusive cryovolcanism on Europa: the post-Galileo perspective. J Geophys Res Planets 108:5139. https://doi.org/10.1029/2003JE002128

Fagents SA, Lopes RMC, Quick LC, Gregg TKP (2022) Cryovolcanism. In: Gregg TKP, Lopes RMC, Fagents SA (eds) Planetary volcanism across the Solar System. Elsevier, Amsterdam, pp 161–234. https://doi.org/10.1016/B978-0-12-813987-5.00005-5

Filacchione G, Ciarniello M, D'Aversa E, Capaccioni F, Clark RN, Buratti BJ, Helfenstein P, Stephan K, Plainaki C (2022) Saturn's icy satellites investigated by Cassini - VIMS. V. Spectrophotometry. Icarus 375:114803. https://doi.org/10.1016/j.icarus.2021.114803

Flasar FM, Kunde VG, Abbas MM, Achterberg RK, Ade P, Barucci A, Bjoraker GL, Brasunas JC, Calcutt S, Carlson R, Esarsky CJC, Conrath BJ, Coradini A, Courtin R, Coustenis A, Edberg S, Edgington S, Ferrari C, Fouchet T, Gautier D, Gierasch PJ, Grossman K, Irwin P, Jennings DE, Lellouch E, Mamoutkine AA, Marten A, Meyer JP, Nixon CA, Orton GS, Owen TC, Pearl JC, Prangé R, Prangé P, Raulin F, Read PL, Romani PN, Samuelson RE, Segura ME, Showalter MR, Simon-Miller AA, Smith MD, Spencer JR, Spilker LJ, Taylor FW (2004) Exploring the Saturn system in the thermal infrared: the composite infrared spectrometer. Space Sci Rev 115:169–297. https://doi.org/10.1007/s11214-004-1454-9

Giese B, Wagner R, Hussmann H, Neukum G, Perry J, Helfenstein P, Thomas PC (2008) Enceladus: an estimate of heat flux and lithospheric thickness from flexurally supported topography. Geophys Res Lett 35:L24204. https://doi.org/10.1029/2008GL036149

Glein CR, Shock EL (2010) Sodium chloride as a geophysical probe of a subsurface ocean on Enceladus. Geophys Res Lett 37:L09204. https://doi.org/10.1029/2010GL042446

Glein CR, Postberg F, Vance SD (2018) The geochemistry of Enceladus: composition and controls. In: Schenk PM et al (eds) Enceladus and the icy moons of Saturn. The University of Arizona Press, Tucson. https://doi.org/10.2458/azu_uapress_9780816537075-ch003

Goguen JD, Buratti BJ, Brown RH, Clark RN, Nicholson PD, Hedman MM, Howell RR, Sotin C, Cruikshank DP, Baines KH, Lawrence KJ, Spencer JR, Blackburn DG (2013) The temperature and width of an active fissure on Enceladus measured with Cassini VIMS during the 14 April 2012 South Pole flyover. Icarus 226:1128–1137. https://doi.org/10.1016/j.icarus.2013.07.012

Hansen CJ, Kirk RL (2015) Triton's plumes–solar driven like Mars or endogenic like Enceladus? In: 46th Lunar and Planetary Science Conference, p 1832

Hansen CJ, McEwen AS, Ingersoll AP, Terrile RJ (1990) Surface and airborne evidence for plumes and winds on Triton. Science 1979(250):421–424. https://doi.org/10.1126/science.250.4979.421

Hansen CJ, Esposito L, Stewart AIF, Colwell J, Hendrix A, Pryor W, Shemansky D, Wast R (2006) Enceladus' water vapor plume. Science 1979(311):1422–1425. https://doi.org/10.1126/science.1121254

Hansen CJ, Esposito LW, Stewart AIF, Meinke B, Wallis B, Colwell JE, Hendrix AR, Larsen K, Pryor W, Tian F (2008) Water vapour jets inside the plume of gas leaving Enceladus. Nature 456:477–479. https://doi.org/10.1038/nature07542

Hansen CJ, Shemansky DE, Esposito LW, Stewart AIF, Lewis BR, Colwell JE, Hendrix AR, West RA, Waite JH, Teolis B, Magee BA (2011) The composition and structure of the Enceladus plume. Geophys Res Lett 38:L11202. https://doi.org/10.1029/2011GL047415

Hansen CJ, Esposito LW, Aye KM, Colwell JE, Hendrix AR, Portyankina G, Shemansky D (2017) Investigation of diurnal variability of water vapor in Enceladus' plume by the Cassini ultraviolet imaging spectrograph. Geophys Res Lett 44:672–677. https://doi.org/10.1002/2016GL071853

Hansen CJ, Castillo-Rogez J, Grundy W, Hofgartner JD, Martin ES, Mitchell K, Nimmo F, Nordheim TA, Paty C, Quick LC, Roberts JH, Runyon K, Schenk P, Stern A, Umurhan O (2021) Triton: fascinating moon, likely ocean world, compelling destination! Planet Sci J 2:137. https://doi.org/10.3847/PSJ/abffd2

Hayne PO, Aharonson O (2015) Thermal stability of ice on Ceres with rough topography. J Geophys Res Planets 120:1567–1584. https://doi.org/10.1002/2015JE004887

Hedman MM, Nicholson PD, Showalter MR, Brown RH, Buratti BJ, Clark RN (2009) Spectral observations of the Enceladus plume with Cassini-vims. Astrophys J 693:1749–1762. https://doi.org/10.1088/0004-637X/693/2/1749

Hedman MM, Gosmeyer CM, Nicholson PD, Sotin C, Brown RH, Clark RN, Baines KH, Buratti BJ, Showalter MR (2013) An observed correlation between plume activity and tidal stresses on Enceladus. Nature 500:182–184. https://doi.org/10.1038/nature12371

Hedman MM, Dhingra D, Nicholson PD, Hansen CJ, Portyankina G, Ye S, Dong Y (2018) Spatial variations in the dust-to-gas ratio of Enceladus' plume. Icarus 305:123–138. https://doi.org/10.1016/j.icarus.2018.01.006

Helfenstein P, Porco CC (2015) Enceladus' geysers: relation to geological features. Astron J 150:96. https://doi.org/10.1088/0004-6256/150/3/96

Helfenstein P, Veverka J, McCarthy D, Lee P, Hillier J (1992) Large quasi-circular features beneath frost on Triton. Science 1979(255):824–826. https://doi.org/10.1126/science.255.5046.824

Hemingway DJ, Mittal T (2019) Enceladus's ice shell structure as a window on internal heat production. Icarus 332:111–131. https://doi.org/10.1016/j.icarus.2019.03.011

Hill TW, Thomsen MF, Tokar RL, Coates AJ, Lewis GR, Young DT, Crary FJ, Baragiola RA, Johnson RE, Dong Y, Wilson RJ, Jones GH, Wahlund J-E, Mitchell DG, Horányi M (2012) Charged nanograins in the Enceladus plume. J Geophys Res Space Phys. https://doi.org/10.1029/2011JA017218

Hofgartner JD, Birch SPD, Castillo J, Grundy WM, Hansen CJ, Hayes AG, Howett CJA, Hurford TA, Martin ES, Mitchell KL, Nordheim TA, Poston MJ, Prockter LM, Quick LC, Schenk P, Schindhelm RN, Umurhan OM (2022) Hypotheses for Triton's plumes: new analyses and future remote sensing tests. Icarus 375:114835. https://doi.org/10.1016/j.icarus.2021.114835

Howett CJA, Spencer JR, Pearl J, Segura M (2010) Thermal inertia and bolometric Bond albedo values for Mimas, Enceladus, Tethys, Dione, Rhea and Iapetus as derived from Cassini/CIRS measurements. Icarus 206:573–593. https://doi.org/10.1016/j.icarus.2009.07.016

Howett CJA, Spencer JR, Pearl J, Segura M (2011) High heat flow from Enceladus' south polar region measured using 10-600 cm-1 Cassini/CIRS data. J Geophys Res E, Planets 116:E03003. https://doi.org/10.1029/2010JE003718

Howett C, Spencer J, Spencer D, Verbiscer A, Hurford T, Segura M (2013) Enceladus' enigmatic heat flow. In: American geophysical union, fall meeting. Abstract Id.P53E-06

Howett C.J.A, Spencer J.R., Hurford T, Verbiscer A, Segura M (2016) Thermal properties of Rhea's poles: evidence for a meter-deep unconsolidated subsurface layer. Icarus 272:140–148. https://doi.org/10.1016/j.icarus.2016.02.033

Howett CJA, Spencer JR, Hurford T, Verbiscer A, Segura M (2019) Maps of Tethys' thermophysical properties. Icarus 321:705–714. https://doi.org/10.1016/j.icarus.2018.12.018

Howett C, Nimmo F, Spencer J (2022) Constraining Enceladus' heat flow between its tiger stripes. In: Europlanet Science Congress, EPSC2022-219. https://doi.org/10.5194/epsc2022-219

Hsu H-W, Postberg F, Sekine Y, Shibuya T, Kempf S, Horányi M, Juhász A, Altobelli N, Suzuki K, Masaki Y, Kuwatani T, Tachibana S, Sirono S, Moragas-Klostermeyer G, Srama R (2015) Ongoing hydrothermal activities within Enceladus. Nature 519:207–210. https://doi.org/10.1038/nature14262

Hurford TA, Helfenstein P, Hoppa GV, Greenberg R, Bills BG (2007) Eruptions arising from tidally controlled periodic openings of rifts on Enceladus. Nature 447:292–294. https://doi.org/10.1038/nature05821

Hurley DM, Perry ME, Waite JH (2015) Modeling insights into the locations of density enhancements from the Enceladus water vapor jets. J Geophys Res Planets 120:1763–1773. https://doi.org/10.1002/2015JE004872

Iess L, Stevenson DJ, Parisi M, Hemingway D, Jacobson RA, Lunine JI, Nimmo F, Armstrong JW, Asmar SW, Ducci M, Tortora P (2015) The gravity field and interior structure of Enceladus. Science 1979(344):78–80. https://doi.org/10.1126/science.1250551

Ingersoll AP, Ewald SP (2011) Total particulate mass in Enceladus plumes and mass of Saturn's E ring inferred from Cassini ISS images. Icarus 216:492–506. https://doi.org/10.1016/j.icarus.2011.09.018

Ingersoll AP, Ewald SP (2017) Decadal timescale variability of the Enceladus plumes inferred from Cassini images. Icarus 282:260–275. https://doi.org/10.1016/j.icarus.2016.09.018

Ingersoll AP, Pankine AA (2010) Subsurface heat transfer on Enceladus: conditions under which melting occurs. Icarus 206:594–607. https://doi.org/10.1016/j.icarus.2009.09.015

Ingersoll AP, Ewald SP, Trumbo SK (2020) Time variability of the Enceladus plumes: orbital periods, decadal periods, and aperiodic change. Icarus 344:113345. https://doi.org/10.1016/j.icarus.2019.06.006

Johnson RE, Smith HT, Tucker OJ, Liu M, Burger MH, Sittler EC, Tokar RL (2006) The Enceladus and OH Tori at Saturn. Astrophys J 644:L137–L139. https://doi.org/10.1086/505750

Jones GH, Arridge CS, Coates AJ, Lewis GR, Kanani S, Wellbrock A, Young DT, Crary FJ, Tokar RL, Wilson RJ, Hill TW, Johnson RE, Mitchell DG, Schmidt J, Kempf S, Beckmann U, Russell CT, Jia YD, Dougherty MK, Waite JH, Magee BA (2009) Fine jet structure of electrically charged grains in Enceladus' plume. Geophys Res Lett 36:L16204. https://doi.org/10.1029/2009GL038284

Jurac S, Richardson JD (2001) The dependence of plasma and magnetic field correlations in the solar wind on geomagnetic activity. J Geophys Res Space Phys 106:29195–29205. https://doi.org/10.1029/2000JA000180

Kattenhorn SA, Prockter LM (2014) Evidence for subduction in the ice shell of Europa. Nat Geosci 7:762–767. https://doi.org/10.1038/ngeo2245

Kempf S, Beckmann U, Moragas-Klostermeyer G, Postberg F, Srama R, Economou T, Schmidt J, Spahn F, Grün E (2008) The E ring in the vicinity of Enceladus. I. Spatial distribution and properties of the ring particles. Icarus 193:420–437. https://doi.org/10.1016/j.icarus.2007.06.027

Kempf S, Beckmann U, Schmidt J (2010) How the Enceladus dust plume feeds Saturn's E ring. Icarus 206:446–457. https://doi.org/10.1016/j.icarus.2009.09.016

Kempf S, Horányi M, Hsu H-W, Hill TW, Juhász A, Smith HT (2018) Saturn's diffuse E ring and its connection with Enceladus. In: Schenk PM et al (eds) Enceladus and the icy moons of Saturn. The University of Arizona Press, Tucson. https://doi.org/10.2458/azu_uapress_9780816537075-ch010

Khawaja N, Postberg F, Schmidt J (2017) The compositional profile of the enceladian ice plume from the latest Cassini flybys. In: Lunar and Planetary Science Conference. Lunar and Planetary Science Institute, Houston, p 2005

Kieffer SW, Lu X, Bethke CM, Spencer JR, Marshak S, Navrotsky A (2006) A clathrate reservoir hypothesis for Enceladus' South Polar plume. Science 1979(314):1764–1766. https://doi.org/10.1126/science.1133519

Kirchoff MR, Schenk P (2010) Global impact cratering record of Saturn's moon dione: constraining the geological history. In: 41st Lunar and Planetary Science Conference

Kirk RL, Soderblom LA, Brown RH, Kieffer S, Kargel W (1995) Triton's plumes: discovery, characteristics and models. In: Cruikshank DP (ed) Neptune and Triton. The University of Arizona Press, Tucson, p 949

Krimigis SM, Mitchell DG, Hamilton DC, Livi S, Dandouras J, Jaskulek S, Armstrong TP, Boldt JD, Cheng AF, Gloeckler G, Hayes JR, Hsieh KC, Ip W-H, Keath EP, Kirsch E, Krupp N, Lanzerotti LJ, Lundgren R, Mauk BH, McEntire RW, Roelof EC, Schlemm CE, Tossman BE, Wilken B, Williams DJ (2004) Magnetosphere Imaging Instrument (MIMI) on the Cassini mission to Saturn/Titan. Space Sci Rev 114:233–329. https://doi.org/10.1007/s11214-004-1410-8

Lainey V, Jacobson RA, Tajeddine R, Cooper NJ, Murray C, Robert V, Tobie G, Guillot T, Mathis S, Remus F, Desmars J, Arlot JE, De Cuyper JP, Dehant V, Pascu D, Thuillot W, Le Poncin-Lafitte C, Zahn JP (2017) New constraints on Saturn's interior from Cassini astrometric data. Icarus 281:286–296. https://doi.org/10.1016/j.icarus.2016.07.014

Lainey V, Casajus LG, Fuller J, Zannoni M, Tortora P, Cooper N, Murray C, Modenini D, Park RS, Robert V, Zhang Q (2020) Resonance locking in giant planets indicated by the rapid orbital expansion of Titan. Nat Astron 4:1053–1058. https://doi.org/10.1038/s41550-020-1120-5

Lainey V, et al (2025) Space Sci Rev 221

Le Gall A, Leyrat C, Janssen MA, Choblet G, Tobie G, Bourgeois O, Lucas A, Sotin C, Howett C, Kirk R, Lorenz RD, West RD, Stolzenbach A, Massé M, Hayes AH, Bonnefoy L, Veyssière G, Paganelli F (2017) Thermally anomalous features in the subsurface of Enceladus's South Polar Terrain. Nat Astron 1:0063. https://doi.org/10.1038/s41550-017-0063

Le Gall A, Bonnefoy LE, Sultana R, Leyrat C, Janssen MA, Wall S, Lellouch E (2023) Microwaving Mimas, Enceladus, Tethys, Dione, Rhea, Iapetus and Phoebe: insights into the regolith properties and geological history of Saturn's icy satellites. Icarus 394:115446. https://doi.org/10.1016/j.icarus.2023.115446

Lesage E, Schmidt F, Andrieu F, Massol H (2021) Constraints on effusive cryovolcanic eruptions on Europa using topography obtained from Galileo images. Icarus 361:114373. https://doi.org/10.1016/j.icarus.2021.114373

Loeffler MJ, Baragiola RA (2009) Physical and chemical effects on crystalline H_2O_2 induced by 20 keV protons. J Chem Phys 130:114504. https://doi.org/10.1063/1.3079612

Magee BA, Waite H (2017) Neutral gas composition of Enceladus' plume – model parameter insights from Cassini-INMS. In: Lunar and planetary science XLVIII, p 2974

Magee B, Waite H (2020) Analysis of minor and trace organic species in Enceladus' plume gas. In: American geophysical union, fall meeting, p #P003-0003

Manga M, Wang C-Y (2007) Pressurized oceans and the eruption of liquid water on Europa and Enceladus. Geophys Res Lett 34:L07202. https://doi.org/10.1029/2007GL029297

McKinnon WB (2015) Effect of Enceladus's rapid synchronous spin on interpretation of Cassini gravity. Geophys Res Lett 42:2137–2143. https://doi.org/10.1002/2015GL063384

Meyer J (2008) Tidal evolution of Mimas, Enceladus and Dione. Icarus 193:213–223. https://doi.org/10.1016/j.icarus.2007.09.008s

Meyer J, Wisdom J (2007) Tidal heating in Enceladus. Icarus 188:535–539. https://doi.org/10.1016/j.icarus.2007.03.001

Miles GM, Howett CJA, Spencer JR (2022) Constraining Enceladus' energy emission outside the South Polar Terrain. In: Europlanet Science Congress, EPSC2022-1190. https://doi.org/10.5194/epsc2022-1190

Miyamoto H, Mitri G, Showman AP, Dohm JM (2005) Putative ice flows on Europa: geometric patterns and relation to topography collectively constrain material properties and effusion rates. Icarus 177:413–424. https://doi.org/10.1016/j.icarus.2005.03.014

Morooka MW, Wahlund J-E, Eriksson AI, Farrell WM, Gurnett DA, Kurth WS, Persoon AM, Shafiq M, André M, Holmberg MKG (2011) Dusty plasma in the vicinity of Enceladus. J Geophys Res Space Phys 116:A12221. https://doi.org/10.1029/2011JA017038

Nakajima M, Ingersoll AP (2016) Controlled boiling on Enceladus. 1. Model of the vapor-driven jets. Icarus 272:309–318. https://doi.org/10.1016/j.icarus.2016.02.027

National Academies of Sciences, Engineering, and Medicine (2022) Origins, worlds, and life: a decadal strategy for planetary science and astrobiology 2023–2032. National Academies Press, Washington DC. https://doi.org/10.17226/26522

Nimmo F, Spencer JR (2015) Powering Triton's recent geological activity by obliquity tides: implications for Pluto geology. Icarus 246:2–10. https://doi.org/10.1016/j.icarus.2014.01.044

Nimmo F, Spencer JR, Pappalardo RT, Mullen ME (2007) Shear heating as the origin of the plumes and heat flux on Enceladus. Nature 447:289–291. https://doi.org/10.1038/nature05783

Nimmo F, Porco C, Mitchell C (2014) Tidally modulated eruptions on Enceladus: Cassini ISS observations and models. Astron J 148:46. https://doi.org/10.1088/0004-6256/148/3/46

Nimmo F, Neveu M, Howett C.J.A (2023) Origin and evolution of Enceladus's tidal dissipation. Space Sci Rev 219:7. https://doi.org/10.1007/s11214-023-01007-4

Paganini L, Villanueva GL, Roth L, Mandell AM, Hurford TA, Retherford KD, Mumma MJ (2019) A measurement of water vapour amid a largely quiescent environment on Europa. Nat Astron 4:266–272. https://doi.org/10.1038/s41550-019-0933-6

Park RS, Mastrodemos N, Jacobson RA, Berne A, Vaughan AT, Hemingway DJ, Leonard EJ, Castillo-Rogez JC, Cockell CS, Keane JT, Konopliv AS, Nimmo F, Riedel JE, Simons M, Vance S (2024) The global shape, gravity field, and libration of Enceladus. J Geophys Res Planets 129:e2023JE008054. https://doi.org/10.1029/2023JE008054

Perry ME, Teolis BD, Hurley DM, Magee BA, Waite JH, Brockwell TG, Perryman RS, McNutt RL (2015) Cassini INMS measurements of Enceladus plume density. Icarus 257:139–162. https://doi.org/10.1016/j.icarus.2015.04.037

Phillips CB, McEwen AS, Hoppa GV, Fagents SA, Greeley R, Klemaszewski JE, Pappalardo RT, Klaasen KP, Breneman HH (2000) The search for current geologic activity on Europa. J Geophys Res Planets 105:22579–22597. https://doi.org/10.1029/1999JE001139

Porco CC, Helfenstein P, Thomas PC, Ingersoll AP, Wisdom J, West R, Neukum G, Denk T, Wagner R, Roatsch T, Kieffer S, Turtle E, Mcewen A, Johnson TV, Rathbun J, Veverka J, Wilson D, Perry J, Spitale J, Brahic A, Burns JA, Delgenio AD, Dones L, Murray CD, Squyres S (2006a) Cassini observes the active South Pole of Enceladus. Science 311:1393–1401. https://doi.org/10.1126/science.1123013

Porco C, West RA, Squyres S, Mcewen A, Thomas P, Murray CD, Delgenio A, Ingersoll AP, Johnson TV, Neukum G, Veverka J, Dones L, Brahic A, Burns JA, Haemmerle V, Knowles B, Dawson D, Roatsch T, Beurle K, Owen W (2006b) Cassini imaging science: instrument characteristics and anticipated scientific investigations at Saturn. Space Sci Rev 115:363–497. https://doi.org/10.1007/s11214-004-1456-7

Porco C, Dinino D, Nimmo F (2014) How the geysers, tidal stresses, and thermal emission across the South Polar Terrain of Enceladus are related. Astron J 148:45. https://doi.org/10.1088/0004-6256/148/3/45

Porco C, Mitchell C, Nimmo F, Tiscareno M (2018) Enceladus' plume temporal variability from analysis of Cassini ISS images. In: 49th Lunar and Planetary Science Conference

Postberg F, Kempf S, Srama R, Green SF, Hillier JK, McBride N, Grün E (2006) Composition of Jovian dust stream particles. Icarus 183:122–134. https://doi.org/10.1016/j.icarus.2006.02.001

Postberg F, Kempf S, Hillier JK, Srama R, Green SF, McBride N, Grün E (2008) The E-ring in the vicinity of Enceladus. II. Probing the moon's interior-the composition of E-ring particles. Icarus 193:438–454. https://doi.org/10.1016/j.icarus.2007.09.001

Postberg F, Kempf S, Schmidt J, Brilliantov N, Beinsen A, Abel B, Buck U, Srama R (2009) Sodium salts in E-ring ice grains from an ocean below the surface of Enceladus. Nature 459:1098–1101. https://doi.org/10.1038/nature08046

Postberg F, Schmidt J, Hillier J, Kempf S, Srama R (2011) A salt-water reservoir as the source of a compositionally stratified plume on Enceladus. Nature 474:620–622. https://doi.org/10.1038/nature10175

Postberg F, Clark RN, Hansen CJ, Coates AJ, Dalle Ore CM, Scipioni F, Hedman MM, Waite JH (2018) Plume and surface composition of Enceladus. In: Schenk PM et al (eds) Enceladus and the icy moons of Saturn. The University of Arizona Press, Tucson. https://doi.org/10.2458/azu_uapress_9780816537075-ch007

Prockter LM, Shirley JH, Dalton JB, Kamp L (2017) Surface composition of pull-apart bands in Argadnel Regio, Europa: evidence of localized cryovolcanic resurfacing during basin formation. Icarus 285:27–42. https://doi.org/10.1016/j.icarus.2016.11.024

Quick LC, Hedman MM (2020) Characterizing deposits emplaced by cryovolcanic plumes on Europa. Icarus 343:113667. https://doi.org/10.1016/j.icarus.2020.113667

Quick LC, Barnouin OS, Prockter LM, Patterson GW (2013) Constraints on the detection of cryovolcanic plumes on Europa. Planet Space Sci 86:1–9. https://doi.org/10.1016/j.pss.2013.06.028

Quick LC, Glaze LS, Baloga SM (2017) Cryovolcanic emplacement of domes on Europa. Icarus 284:477–488. https://doi.org/10.1016/j.icarus.2016.06.029

Quick LC, Fagents SA, Núñez KA, Wilk KA, Beyer RA, Beddingfield CB, Martin ES, Prockter LM, Hurford TA (2022) Cryolava dome growth resulting from active eruptions on Jupiter's moon Europa. Icarus 387:115185. https://doi.org/10.1016/j.icarus.2022.115185

Rhoden AR, Hurford TA, Roth L, Retherford K (2015) Linking Europa's plume activity to tides, tectonics, and liquid water. Icarus 253:169–178. https://doi.org/10.1016/j.icarus.2015.02.023

Roth L, Retherford KD, Saur J, Strobel DF, Feldman PD, McGrath MA, Nimmo F (2014a) Orbital apocenter is not a sufficient condition for HST/STIS detection of Europa's water vapor aurora. Proc Natl Acad Sci USA 111:E5123. https://doi.org/10.1073/pnas.1416671111

Roth L, Saur J, Retherford KD, Strobel DF, Feldman PD, McGrath MA, Nimmo F (2014b) Transient water vapor at Europa's South Pole. Science 1979(343):171–174. https://doi.org/10.1126/science.1247051

Schenk PM (2020) The search for Europa's plumes: no surface patterns or changes 1979–2007? Astrophys J 892:L12. https://doi.org/10.3847/2041-8213/ab6f78

Schenk PM, McKinnon WB (2009) One-hundred-km-scale basins on Enceladus: evidence for an active ice shell. Geophys Res Lett 36:L16202. https://doi.org/10.1029/2009GL039916

Schenk P, Hamilton DP, Johnson RE, McKinnon WB, Paranicas C, Schmidt J, Showalter MR (2011) Plasma, plumes and rings: Saturn system dynamics as recorded in global color patterns on its midsize icy satellites. Icarus 211:740–757. https://doi.org/10.1016/j.icarus.2010.08.016

Schmidt J, Brilliantov N, Spahn F, Kempf S (2008) Slow dust in Enceladus' plume from condensation and wall collisions in tiger stripe fractures. Nature 451:685–688. https://doi.org/10.1038/nature06491

Schmidt BE, Blankenship DD, Patterson GW, Schenk PM (2011) Active formation of 'chaos terrain' over shallow subsurface water on Europa. Nature 479:502–505. https://doi.org/10.1038/nature10608

Schubert G, Anderson JD, Travis BJ, Palguta J (2007) Enceladus: present internal structure and differentiation by early and long-term radiogenic heating. Icarus 188:345–355. https://doi.org/10.1016/j.icarus.2006.12.012

Scipioni F, Schenk P, Tosi F, D'Aversa E, Clark R, Combe J-P, Ore CMD (2017) Deciphering sub-micron ice particles on Enceladus surface. Icarus 290:183–200. https://doi.org/10.1016/j.icarus.2017.02.012

Sekine Y, Shibuya T, Postberg F, Hsu H-W, Suzuki K, Masaki Y, Kuwatani T, Mori M, Hong PK, Yoshizaki M, Tachibana S, Sirono S (2015) High-temperature water–rock interactions and hydrothermal environments in the chondrite-like core of Enceladus. Nat Commun 6:8604. https://doi.org/10.1038/ncomms9604

Soderblom LA, Kieffer SW, Becker TL, Brown RH, Cook AF, Hansen CJ, Johnson TV, Kirk RL, Shoemaker EM (1990) Triton's geyser-like plumes: discovery and basic characterization. Science 1979(250):410–415. https://doi.org/10.1126/science.250.4979.410

Southworth BS, Kempf S, Spitale J (2019) Surface deposition of the Enceladus plume and the zenith angle of emissions. Icarus 319:33–42. https://doi.org/10.1016/j.icarus.2018.08.024

Spahn F, Schmidt J, Albers N, Hörning M, Makuch M, Seiß M, Kempf S, Srama R, Dikarev V, Helfert S, Moragas-Klostermeyer G, Krivov AV, Sremčević M, Tuzzolino AJ, Economou T, Grün E (2006) Cassini dust measurement at Enceladus and implications for the origin of the E ring. Science 1979(311):1416–1418. https://doi.org/10.1126/science.1121375

Sparks WB, Hand KP, McGrath MA, Bergeron E, Cracraft M, Deustua SE (2016) Probing for evidence of plumes on Europa with HST/STIS. Astrophys J 829:121. https://doi.org/10.3847/0004-637X/829/2/121

Sparks WB, Schmidt BE, McGrath MA, Hand KP, Spencer JR, Cracraft M, Deustua SE (2017) Active cryovolcanism on Europa? Astrophys J 839:L18. https://doi.org/10.3847/2041-8213/aa67f8

Spencer JR, Lebofskyf LA, Sykes MV (1989) Systematic biases in radiometric diameter determinations. Icarus 78:337–354. https://doi.org/10.1016/0019-1035(89)90182-6

Spencer JR, Pearl JC, Segura M, Flasar FM, Mamoutkine A, Romani P, Buratti BJ, Hendrix AR, Spilker LJ, Lopes RMC (2006) Cassini encounters Enceladus: background and the discovery of a south polar hot spot. Science 1979(311):1401–1405. https://doi.org/10.1126/science.1121661

Spencer J, Nimmo F, Ingersoll AP, Hurford TA, Kite ES, Rhoden AR, Schmidt J, Howett CJA (2018) Plume origins and plumbing (ocean to surface). In: Schenk PM et al (eds) Enceladus and the icy moons of Saturn. The University of Arizona Press, Tucson. https://doi.org/10.2458/azu_uapress_9780816537075-ch008

Spitale JN, Porco CC (2007) Association of the jets of Enceladus with the warmest regions on its south-polar fractures. Nature 449:695–697. https://doi.org/10.1038/nature06217

Spitale JN, Hurford TA, Rhoden AR, Berkson EE, Platts SS (2015) Curtain eruptions from Enceladus'south-polar terrain. Nature 521:57–60. https://doi.org/10.1038/nature14368

Spohn T, Schubert G (2003) Oceans in the icy Galilean satellites of Jupiter? Icarus. https://doi.org/10.1016/S0019-1035(02)00048-9

Srama R, Ahrens TJ, Altobelli N, Auer S, Bradley JG, Burton M, Dikarev VV, Economou T, Fechtig H, Görlich M, Grande M, Graps A, Grün E, Havnes O, Helfert S, Horanyi M, Igenbergs E, Jessberger EK, Johnson TV, Kempf S, Krivov AV, Krüger H, Mocker-Ahlreep A, Moragas-Klostermeyer G, Lamy P, Landgraf M, Linkert D, Linkert G, Lura F, McDonnell JAM, Möhlmann D, Morfill GE, Müller M, Roy M, Schäfer G, Schlotzhauer G, Schwehm GH, Spahn F, Stübig M, Svestka J, Tschernjawski V, Tuzzolino AJ, Wäsch R, Zook HA (2004) The Cassini cosmic dust analyzer. Space Sci Rev 114:465–518. https://doi.org/10.1007/s11214-004-1435-z

Teolis BD, Perry ME, Hansen CJ, Waite JH, Porco CC, Spencer JR, Howett CJA (2017) Enceladus plume structure and time variability: comparison of Cassini observations. Astrobiology 17:926–940. https://doi.org/10.1089/ast.2017.1647

Thomas N, Portyankina G, Hansen CJ, Pommerol A (2011) HiRISE observations of gas sublimation-driven activity in Mars' southern polar regions: IV. Fluid dynamics models of CO_2 jets. Icarus 212:66–85. https://doi.org/10.1016/j.icarus.2010.12.016

Thomas PC, Tajeddine R, Tiscareno MS, Burns JA, Joseph J, Loredo TJ, Helfenstein P, Porco C (2016) Enceladus's measured physical libration requires a global subsurface ocean. Icarus 263:37–47. https://doi.org/10.1016/j.icarus.2015.08.037

Tokar RL, Johnson RE, Hill TW, Pontius DH, Kurth WS, Crary FJ, Young DT, Thomsen MF, Reisenfeld DB, Coates AJ, Lewis GR, Sittler EC, Gurnett DA (2006) The interaction of the atmosphere of Enceladus with Saturn's plasma. Science 1979(311):1409–1412. https://doi.org/10.1126/science.1121061

Travis BJ, Schubert G (2015) Keeping Enceladus warm. Icarus 250:32–42. https://doi.org/10.1016/j.icarus.2014.11.017

USGS (2015) Enceladus Nomenclature [WWW Document]. https://planetarynames.wr.usgs.gov/images/enceladus_comp.pdf

Verbiscer A, French R, Showalter M, Helfenstein P (2007) Enceladus: cosmic graffiti artist caught in the act. Science. https://doi.org/10.1126/science.1134681

Villaneuva GL, Hammel HB, Milam SN, Faggi S, Kofman V, Roth L, Hand KP, Paganini L, Stansberry J, Spencer J, Protopapa S, Strazzulla G, Cruz-Mermy G, Glein CR, Cartwright R, Liuzzi G (2023) Endogenous CO_2 ice mixture on the surface of Europa and no detection of plume activity. Science 381:1305–1308. https://doi.org/10.1126/science.adg4270

Waite JH, Lewis WS, Kasprzak WT, Anicich VG, Block BP, Cravens TE, Fletcher GG, Ip W-H, Luhmann JG, Mcnutt RL, Niemann HB, Parejko JK, Richards JE, Thorpe RL, Walter EM, Yelle RV (2004) The Cassini Ion and Neutral Mass Spectrometer (INMS) investigation. Space Sci Rev 114:113–231. https://doi.org/10.1007/s11214-004-1408-2

Waite JH, Combi MR, Ip WH, Cravens TE, McNutt RL, Kasprzak W, Yelle R, Luhmann J, Niemann H, Gell D, Magee B, Fletcher G, Lunine J, Tseng WL (2006) Cassini ion and Neutral Mass Spectrometer: Enceladus plume composition and structure. Science 1979(311):1419–1422. https://doi.org/10.1126/science.1121290

Waite JH, Glein CR, Perryman RS, Teolis BD, Magee BA, Miller G, Grimes J, Perry ME, Miller KE, Bouquet A, Lunine JI, Brockwell T, Bolton SJ (2017) Cassini finds molecular hydrogen in the Enceladus plume: evidence for hydrothermal processes. Science 1979(356):155–159. https://doi.org/10.1126/science.aai8703

Yeoh SK, Chapman TA, Goldstein DB, Varghese PL, Trafton LM (2015) On understanding the physics of the Enceladus south polar plume via numerical simulation. Icarus 253:205–222. https://doi.org/10.1016/j.icarus.2015.02.020

Young DT, Berthelier JJ, Blanc M, Burch JL, Coates AJ, Goldstein R, Grande M, Hill TW, Johnson RE, Kelha V, Mccomas DJ, Sittler EC, Svenes KR, Szegö K, Tanskanen P, Ahola K, Anderson D, Bakshi S, Baragiola RA, Barraclough BL, Black RK, Bolton S, Booker T, Bowman R, Casey P, Crary FJ, Delapp D, Dirks G, Eaker N, Funsten H, Furman JD, Gosling JT, Hannula H, Holmlund C, Huomo H, Illiano JM, Jensen P, Johnson MA, Linder DR, Luntama T, Maurice S, Mccabe KP, Mursula K, Narheim BT, Nordholt JE, Preece A, Rudzki J, Ruitberg A, Smith K, Szalai S, Thomsen MF, Viherkanto K, Vilppola J, Vollmer T, Wahl TE, Wüest M, Ylikorpi T, Zinsmeyer C (2004) Cassini plasma spectrometer investigation. Space Sci Rev 114:1–112. https://doi.org/10.1007/s11214-004-1406-4

Young DT, Berthelier J-J, Blanc M, Burch JL, Bolton S, Coates AJ, Crary FJ, Goldstein R, Grande M, Hill TW, Johnson RE, Baragiola RA, Kelha V, McComas DJ, Mursula K, Sittler EC, Svenes KR, Szegö K, Tanskanen P, Thomsen MF, Bakshi S, Barraclough BL, Bebesi Z, Delapp D, Dunlop MW, Gosling JT, Furman JD, Gilbert LK, Glenn D, Holmlund C, Illiano J-M, Lewis GR, Linder DR, Maurice S, McAndrews HJ, Narheim BT, Pallier E, Reisenfeld D, Rymer AM, Smith HT, Tokar RL, Vilppola J, Zinsmeyer C (2005) Composition and dynamics of plasma in Saturn's magnetosphere. Science 307:1262–1266. https://doi.org/10.1126/science.1106151